



# The Large Sky Area Multi-Object Fiber Spectroscopic Telescope (LAMOST) Quasar Survey: Quasar Properties from Data Releases 6 to 9

Jun-Jie Jin<sup>1,2,3</sup> , Xue-Bing Wu<sup>1,2</sup> , Yuming Fu<sup>1,2</sup> , Su Yao<sup>4</sup> , Yan-Li Ai<sup>5,6</sup>, Xiao-Tong Feng<sup>1,2</sup>, Zi-Qi He<sup>1,2</sup>, Qin-Chun Ma<sup>1,2</sup>, Yu-Xuan Pang<sup>1,2</sup>, Rui Zhu<sup>1,2</sup>, Yan-xia Zhang<sup>7</sup>, Hai-long Yuan<sup>7</sup>, and Zhi-Ying Huo<sup>7</sup>

<sup>1</sup> Department of Astronomy, School of Physics, Peking University, Beijing 100871, People's Republic of China; [jjjin@pku.edu.cn](mailto:jjjin@pku.edu.cn), [wuxb@pku.edu.cn](mailto:wuxb@pku.edu.cn)

<sup>2</sup> Kavli Institute for Astronomy and Astrophysics, Peking University, Beijing 100871, People's Republic of China

<sup>3</sup> Key Laboratory of Optical Astronomy, National Astronomical Observatories, Chinese Academy of Sciences, Beijing 100012, People's Republic of China

<sup>4</sup> Max-Planck-Institut für Radioastronomie, Auf dem Hügel 69, D-53121 Bonn, Germany

<sup>5</sup> College of Engineering Physics, Shenzhen Technology University, Shenzhen 518118, People's Republic of China

<sup>6</sup> Shenzhen Key Laboratory of Ultraintense Laser and Advanced Material Technology, Shenzhen 518118, People's Republic of China

<sup>7</sup> National Astronomical Observatories, Chinese Academy of Sciences, Beijing 100012, People's Republic of China

Received 2022 June 24; revised 2022 November 28; accepted 2022 December 11; published 2023 March 7

## Abstract

We report the fourth installment in the series of the Large Sky Area Multi-Object Fiber Spectroscopic Telescope (LAMOST) quasar survey, which includes quasars observed between 2017 September and 2021 June. There are in total 13,066 quasars reliably identified, of which 6685 are newly discovered that are not reported in the Sloan Digital Sky Survey (SDSS) DR14 quasar catalog or Million Quasars catalog. Because LAMOST does not provide accurate absolute flux calibration, we recalibrate the spectra with the SDSS/Pan-STARRS1 multiband photometric data. The emission-line properties of H $\alpha$ , H $\beta$ , Mg II, and C IV and the continuum luminosities are measured by fitting the recalibrated spectra. We also estimate the single-epoch virial black hole masses ( $M_{\text{BH}}$ ) using the derived emission-line and continuum parameters. This is the first time that the emission-line and continuum fluxes were estimated based on LAMOST recalibrated quasar spectra. The catalog and spectra for these quasars are available online. After the 9 yr LAMOST quasar survey, there are in total 56,175 identified quasars, of which 24,127 are newly discovered. The LAMOST quasar survey not only discovers a great number of new quasars but also provides a database for investigating the spectral variability of the quasars observed by both LAMOST and SDSS and finding rare quasars, including changing-look quasars and broad absorption line quasars.

*Unified Astronomy Thesaurus concepts:* Quasars (1319); Catalogs (205); Surveys (1671)

*Supporting material:* machine-readable table

## 1. Introduction

Quasars are a class of active galactic nuclei (AGNs), which are powered by accretion onto the supermassive black holes (SMBHs). Quasars are the most luminous and energetic celestial objects in the universe that can emit radiations over a broad range of wavelength from radio to  $\gamma$ -rays (Antonucci 1993). Quasars have long been used in a variety of astrophysical studies, such as revealing the growth of SMBHs across cosmic time and the evolution connections to their host galaxies (Magorrian et al. 1998; Gebhardt et al. 2000; Ferrarese & Merritt 2000; Kormendy & Gebhardt 2001; Merritt & Ferrarese 2001; Tremaine et al. 2002; Li et al. 2021a, 2021b), probing the distribution of interstellar and intergalactic medium (ISM and IGM), and tracing the large-scale structure of the early universe (Becker et al. 2001; Hennawi & Prochaska 2007). In addition, quasars are primary celestial references because they are distant extragalactic sources with extremely small proper motions (Feissel & Mignard 1998; Andrei et al. 2009).

Since the first discovery of the quasars in 1963 (Schmidt 1963), huge efforts have been undertaken to find more quasars. Quasars can be separated from normal galaxies and stars owing to their unique features, such as the

characteristic spectral energy distribution, high luminosities, variability properties, and radiations at multiple wavelengths.

The most common method to select quasar candidates is based on the multicolor properties. Particularly, quasars at  $z < 2.2$  have strong UV and optical emissions that distinguish them from normal stars in the color–color and color–magnitude diagrams (Fan et al. 2000; Schneider et al. 2007; Richards et al. 2009). For example, two of the most productive quasar surveys, the Sloan Digital Sky Survey (SDSS; Shen et al. 2011; Pâris et al. 2012, 2018) and the Two Degree Field (2dF) Quasar Redshift Survey (Boyle et al. 2000) used the optical photometric data to select quasar candidates. However, such optical color selection methods are systematically incomplete at  $2.2 < z < 3.0$ , especially at  $z = 2.7$ , as the quasars in this redshift range have similar colors to those of stellar objects (Fan 1999; Richards et al. 2002, 2006; Schneider et al. 2007). An efficient way of identifying missing quasars at  $2.2 < z < 3.0$  is using the  $K$ -band photometry from the UK Infrared Telescope (UKIRT) Infrared Deep Sky Survey (UKIDSS; Lawrence et al. 2007), because quasars at  $2.2 < z < 3.0$  have an excess in the near-infrared  $K$  band when compared to stellar objects (Warren et al. 2000; Sharp et al. 2002; Maddox et al. 2008; Smail et al. 2008). Thanks to the larger survey area, the all-sky survey Wide-field Infrared Survey Explorer (WISE; Wright et al. 2010; Cutri et al. 2012) shines more light on quasar surveys. It has been demonstrated that the SDSS/UKIDSS and SDSS/WISE colors can significantly improve the efficiency of quasar selection (Wu & Jia 2010; Wu et al. 2012).



Original content from this work may be used under the terms of the [Creative Commons Attribution 4.0 licence](#). Any further distribution of this work must maintain attribution to the author(s) and the title of the work, journal citation and DOI.

Other main quasar candidate selection techniques based on the physical characteristics of quasars include multiwavelength (X-ray/radio) data matching (Schmidt 1963; Silverman et al. 2002; Carballo et al. 2004; Zeimann et al. 2011; Ai et al. 2016), variability-based selection (MacLeod et al. 2012; Palanque-Delabrouille et al. 2016; Ai et al. 2016), slitless-spectroscopy survey for broad emission line features (Clowes 1986; Worseck et al. 2008), and proper motion (Heintz et al. 2020).

Recently, various data-mining algorithms based on photometric data have also been applied to select quasar candidates, including kernel density estimation (KDE; Richards et al. 2004, 2009), the extreme deconvolution method (XDQSO; Bovy et al. 2011), support vector machine (SVM; Peng et al. 2012), Gaussian mixture model (Bailer-Jones et al. 2019), boosting algorithm (e.g., XGBoost; Jin et al. 2019), and deep learning (Yèche et al. 2010; Pasquet-Itam & Pasquet 2018). For example, the KDE method has been exploited in the SDSS-III Baryon Oscillation Spectroscopic Survey (BOSS; Ross et al. 2012), and transfer learning is adopted for finding quasars behind the Galactic plane (GPQs; Fu et al. 2021).

Quasar candidates selected from various methods still need to be spectroscopically identified. This paper presents the results of the Large Sky Area Multi-Object Fiber Spectroscopic Telescope (LAMOST) quasar survey conducted between 2017 September and 2021 June. This is the fourth installment in the series of LAMOST quasar surveys, after Data Release 1 (DR1; Ai et al. 2016, hereafter Paper I), Data Releases 2 and 3 (DR2 and DR3; Dong et al. 2018, hereafter Paper II), and Data Releases 4 and 5 (DR4 and DR5; Yao et al. 2019, hereafter Paper III). In this paper, the candidate selection, spectroscopic survey, and quasar identification are briefly reviewed in Section 2. Spectral measurements and  $M_{\text{BH}}$  estimations for identified quasars are described in Section 3. The description of the quasar catalog and parameters released are presented in Section 4. Finally, the summary and discussion are given in Section 5. We adopt the cosmology parameter  $H_0 = 70 \text{ km s}^{-1} \text{ Mpc}^{-1}$  and a flat universe with  $\Omega_M = 0.3$  and  $\Omega_\Lambda = 0.7$ .

## 2. Survey Outline

LAMOST, also known as the Guoshoujing Telescope, is a quasi-meridian reflection Schmidt telescope with an effective aperture that varies from 3.6 to 4.9 m (Wang et al. 1996; Su & Cui 2004; Cui et al. 2012; Zhao et al. 2012). It is located at Xinglong Observatory, China, and has a  $5^\circ$  (diameter) field of view. LAMOST is equipped with 4000 fibers with  $3''$  diameter, which are mounted on the focal plane and connected to 16 spectrographs. Each spectrum is divided into a blue channel (3700–5900 Å) and a red channel (5700–9000 Å), with an overlapping region between the two channels at 5700–5900 Å. The spectra were observed under the low-resolution mode with a spectral resolution of  $R \sim 1000$ –2000 over the entire wavelength range.

After the commissioning from 2009 to 2010, LAMOST began a pilot survey in 2011 (Luo et al. 2012). The LAMOST regular survey starts from 2012 September, which has two major parts (Zhao et al. 2012): the LAMOST Experiment for Galactic ExtraGalactic Survey (LEGAS), and the LAMOST Experiment for Galactic Understanding and Exploration survey (LEGUE). The LAMOST quasar survey was conducted under LEGAS. The exposure time is adjusted according to the apparent magnitude of targets and observation conditions. The typical value of the total exposure time for a target is  $\sim 90$

minutes, which is equally divided into three subexposures. Although the LAMOST quasar survey used only a small fraction of the available observing time owing to the limitations of the LAMOST site (e.g., weather conditions, poor seeing, and bright sky background), LAMOST has still collected useful data and identified more than 40,000 quasars, about half of which are new discoveries, during the first 5 yr.

### 2.1. Target Selection

The methods used to select the quasar candidates for the LAMOST quasar survey are described in detail in Wu & Jia (2010), Wu et al. (2012), Peng et al. (2012), and Papers I, II, and III. Here, we just give a brief description of the candidate selection.

The primary selection for quasar candidates is based on the photometric data of SDSS (Ahn et al. 2012), and the magnitudes we used here are the SDSS point-spread function (PSF) magnitudes with the Galactic extinction corrected (Schlegel et al. 1998). First, only point sources are selected to exclude galaxies. We notice that we may miss some quasars at low redshifts with extended morphology owing to this limitation. Second, the targets should be brighter than  $i = 20$  to avoid too low signal-to-noise ratio (S/N), and fainter than  $i = 16$  to avoid saturation and contamination with neighbor fibers. Various methods are then applied to further separate quasar candidates from stars. Most of the quasar candidates are selected based on the optical–infrared colors (SDSS-UKIDSS/WISE), as has been described in Wu & Jia (2010) and Wu et al. (2012). A few data-mining algorithms are also used to select quasar candidates, such as SVM classifiers (Peng et al. 2012), XDQSO (Bovy et al. 2011), and KDE (Richards et al. 2009). In addition, some quasar candidates are selected by cross-matching SDSS photometry with the detected sources in X-ray surveys (XMM-Newton, Chandra, ROSAT) and radio surveys (FIRST, NVSS).

Although some of the selected candidates have already been identified by SDSS after our target selections, we include them in the LAMOST survey, which will be helpful to investigate the spectroscopic variability of quasars and find unusual quasars.

### 2.2. Pipeline for Data Reduction

The raw CCD images obtained from observations were reduced by the LAMOST two-dimensional (2D) pipeline and one-dimensional (1D) pipeline, which are described in Luo et al. (2015). The 2D pipeline is applied to extract 1D spectra from the raw data through a sequence of procedures, including dark and bias subtraction, flat-field correction, cosmic-ray removal, spectral tracing and extraction, sky subtraction, wavelength calibration, merging subexposure, relative flux calibration, and combining blue and red spectra (Luo et al. 2012). Then, through the 1D pipeline, these 1D spectra are automatically classified into four primary categories, “STAR,” “GALAXY,” “QSO,” and “Unknown,” by template matching. The final spectra are available at the LAMOST Data Archive Server.<sup>8</sup>

The 1D pipeline classification is not trustworthy for the “Unknown” type. The main reason is that these “Unknown” spectra are taken under nonphotometric conditions, e.g.,

<sup>8</sup> <http://www.lamost.org/lmusers/>

varying seeing and/or cloudy weather. In addition, unstable efficiencies of some fibers also contribute to the high fraction of “Unknown” objects. In the LAMOST early data release, only  $\sim 14\%$  of the observed quasar candidates are classified as QSO, STAR, or GALAXY by the pipeline, while the majority of the spectra are categorized as “Unknown” (Paper I). Such a high fraction of unrecognizable objects is due to the poor spectral quality in the early data release. Both the varying seeing and the nonclassical dome of the telescope significantly affect the spectral quality, and the targets with magnitude fainter than  $i = 20$  are challenging for the LAMOST LEGAS survey. Fortunately, the candidate selection in the regular survey was improved when compared to those in the pilot survey, and the LAMOST data reduction pipeline has been updated for a better performance of spectral classification. As a result, the fraction of candidates classified as “QSO” remains relatively high in later regular surveys (55.9% in Paper II, 62.3% in Paper III, and 77.0% in this work).

### 2.3. Quasar Identification

In this work, the quasars are identified by visual inspections. In addition to the observed spectra of quasar candidates, the spectra that are classified as “QSO” by the 1D pipeline but not included in the input quasar candidate catalog also need visual inspections. With the help of a Java program ASERA (Yuan et al. 2013), we visually inspect these spectra based on the typical quasar emission lines. Each spectrum is inspected by at least two persons to check whether the spectral features match the quasar template. The objects that are misclassified by the 1D pipeline are rejected or reclassified. The redshift of each identified quasar is determined when one or more available typical quasar emission lines (e.g., as H $\alpha$ , H $\beta$ , O III  $\lambda 5007$ , Mg II, C III, and C IV) are best matched with the templates. The “ZWARNING = 1” flag indicates that there is only one emission line available. The quasars that overlap with M31/M33 and the Galactic-anticenter extension region (GACext) will be published elsewhere (see Huo et al. 2010, 2013, 2015) and are not included in our final quasar catalog. Finally, there are in total 13,066 visually confirmed quasars from Data Release 6 to 9 in the quasar catalog. Of these, 9827 are not included in the LAMOST quasar survey candidate catalog (updated in 2017, and a new version including PS1 quasar candidates is still in preparation) but identified as quasars. Among the 13,066 identified quasars, after excluding known ones in common with the SDSS DR14 quasar catalog or Million Quasars catalog (Milliquas v7.5<sup>9</sup>; Flesch 2021), the remaining 6685 are newly discovered. Since the LAMOST DR6 quasar survey was finished in the same year as the SDSS DR14 quasar catalog was published, the 417 quasars in LAMOST DR6 that are in common with SDSS DR14 are considered as independently discovered by LAMOST. Therefore, there are in total 7102 quasars that were independently discovered by LAMOST. The result of quasar identification is summarized in Table 1. The SDSS DR16 quasar catalog (Lyke et al. 2020) was published in 2020 September, and the observations of most objects in our survey were completed before that. Therefore, we no longer make a comparison between SDSS DR16Q and this work. We caution, however, that 1257 of the newly discovered LAMOST quasars were reported in SDSS DR16Q. With a large number of repeat

**Table 1**  
Results of the LAMOST Quasar Survey in DR6, 7, 8, and 9

	DR6	DR7	DR8	DR9	Total
Total	4275	2294	3883	2614	13,066
Independent	2245	879	2223	1755	7102
New	1828	879	2223	1755	6685

spectral observations of SDSS and LAMOST, we can investigate the spectroscopic variability of quasars on both short and long timescales. Moreover, these multipoch spectra give us a good chance to search for unusual AGNs such as changing-look AGNs (CL-AGNs; e.g., Runcu et al. 2016; Yang et al. 2018; MacLeod et al. 2019; Guo et al. 2019; Wang et al. 2019) and uncover the possible physical mechanism behind them (MacLeod et al. 2019; Frederick et al. 2019; Jin et al. 2022).

Figure 1 shows the distribution of the redshift and absolute luminosity, which is represented by the  $K$ -corrected  $i$ -band absolute magnitude  $M_i(z=2)$ , normalized at  $z = 2$  (Richards et al. 2006). As can be seen, there is a drop in the redshift distribution at  $z \sim 1$ , which is similar to the previous results (Papers I, II, and III). This drop is the result of inefficient identification in this redshift range when the emission line Mg II moves into the overlapping region of the blue and red channels of the spectrograph. For the sources observed by both SDSS and LAMOST, only 88 of them have redshift difference ( $\Delta z = z_{\text{LAMOST}} - z_{\text{SDSS}}$ ) greater than 0.1. The difference mainly comes from the misidentification of emission lines in LAMOST spectra owing to the low S/N. As shown in Figure 2, it is clear that as the S/N decreases the  $\Delta z$  increases. Another reason for the redshift difference is that we estimated the redshift based on the strongest typical emission line, while the redshift values in SDSS are measured with a few different approaches, such as principal component analysis or Mg II emission line (Pâris et al. 2018).

We present the SDSS-WISE/UKIDSS color–color distributions for these identified quasars in Figure 3. It is clear that most (99%) of the identified quasars are located in the selection regions obtained with the optical–infrared color, suggesting that the optical–infrared color selection is a very promising method for selecting quasars. Generally, the quasars uniquely identified by LAMOST are slightly redder in color than those commonly identified by LAMOST and SDSS. The reasons for these color differences may be that the SDSS quasars are mainly selected by optical colors or optical variability (Richards et al. 2002; Morganson et al. 2015; Myers et al. 2015; Palanque-Delabrouille et al. 2016).

## 3. Spectral Analysis

In this section, we describe the spectral analysis, which includes the absolute flux calibration, the measurements of typical quasar emission lines, and the estimations of  $M_{\text{BH}}$ .

### 3.1. Absolute Flux Calibration

We note that LAMOST is designed as a spectroscopic survey without photometric measurements for the observed targets, and there may not be enough standard stars for a given LAMOST field, especially at high Galactic latitude. Thus, this instrument can only provide relative flux calibration rather than absolute flux calibration (Song et al. 2012; Xiang et al. 2015).

<sup>9</sup> <http://www.quasars.org/milliquas.htm>

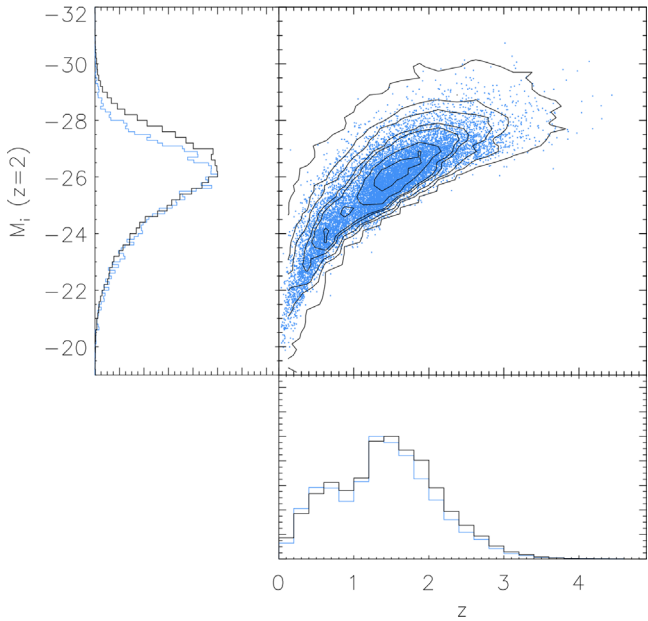


**Figure 1.** The distribution in the magnitude–redshift space for the visually confirmed quasars for the previous LAMOST quasar survey (black contours) and in DR6–DR9 (blue). The absolute magnitudes  $M_i(z = 2)$  are normalized at  $z = 2$ , following the  $K$ -correction of Richards et al. (2006). The left and bottom panels show the absolute magnitude and redshift distributions, respectively.

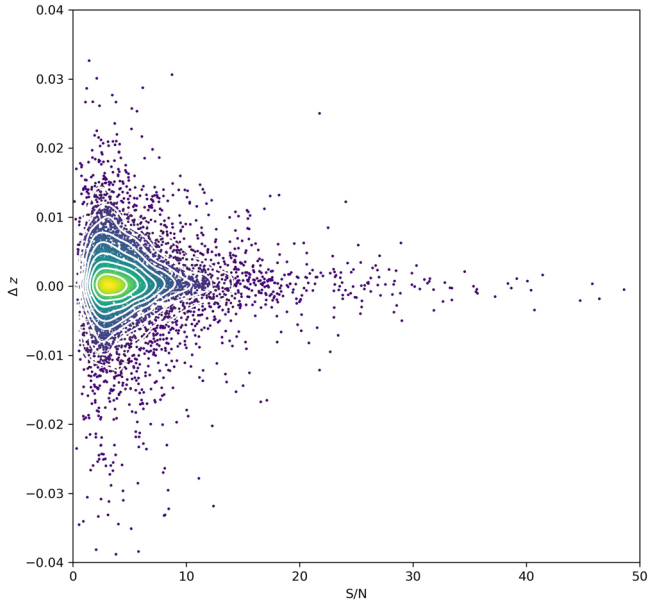


**Figure 2.** The distribution of redshift difference ( $\Delta z$ ) for common quasars between this work and SDSS vs. LAMOST spectral S/N.

As mentioned above, the process of relative flux calibration is the final step of the 2D pipeline. In the first step of relative flux calibration, the A- and F-type stars with high-quality spectra are selected as pseudostandard stars for each spectrograph and are used to calibrate both the blue and red spectrograph arms. The effective temperatures of these stars are estimated using the Lick spectral index grid (Robinson & Wampler 1972; Trager et al. 1998). Then, the spectral response curve (SRC) of each spectrograph is obtained by dividing the observed continuum from the data by the physical pseudocontinuum for the star. Further, these SRCs are applied to all other fiber spectra to

calibrate them. Finally, the red and blue spectra are combined by stacking the points with corresponding wavelength using B-spline function with inverse variance (Song et al. 2012; Luo et al. 2015).

Only with the relative-flux-calibrated spectra can we not estimate the emission-line flux, as well as the continuum luminosity for LAMOST quasars. However, the absolute calibration can be achieved by scaling the relative-flux-calibrated spectra to the photometric measurements (Xiang et al. 2015). In this work, we try to achieve the absolute calibration by scaling each spectrum to the corresponding broadband photometric measurements. The broadband photometry used in this work are the PSF magnitudes from the SDSS (York et al. 2000) or Pan-STARRS1 (Chambers et al. 2016; Flewelling et al. 2020). First, we cross-match the LAMOST quasars with the SDSS photometric database with a  $3''$  matching radius. The sources outside the SDSS footprint are then cross-matched with Pan-STARRS1 with the same matching radius.<sup>10</sup> Due to the limitation of spectral wavelength coverage, we only use  $g$ ,  $r$ , and  $i$  bands during the calibration. The magnitudes in these three bands are converted into the flux density  $f_\lambda$  at the effective wavelength of each filter. Next, we fit each quasar spectrum with the flux densities in the three bands.

Since the spectra from the blue and red channels are relative-flux-calibrated separately in the LAMOST 2D pipeline, the absolute flux calibration is also applied to the blue and red channels separately. The fits are based on the IDL routines in the MPFIT package (Markwardt 2009), which performs the  $\chi^2$  minimization using the Levenberg–Marquardt method. Examples of the fitting results are presented in Figure 4. The released LAMOST spectrum (the gray spectrum in the top panel) only has the relative flux distribution without units. After the absolute flux calibration, the flux density of LAMOST spectrum has units of  $\text{erg cm}^{-2} \text{s}^{-1} \text{\AA}^{-1}$ . Actually, there is only a scale applied to the LAMOST released spectra separately in the blue and red channels corresponding to the  $g$ ,  $r$ , and  $i$  bands, so the spectral shapes in the blue and red channels are not changed during the process.

As we mentioned before, one step in the LAMOST 2D pipeline is connecting the spectra in blue and red channels to each other. However, in some cases, this procedure produces strange shapes in the continuum with a connection defect, which is shown clearly in the top panel of Figure 4 as an example. This defect may cause unpredictable errors in the subsequent spectral fitting process. Fortunately, the strange shapes caused by the defect can be improved by the process of absolute flux calibration as the blue and red channels are reconnected corresponding to the photometry data. As shown in the middle panel of Figure 4, it is clear that the shape of continuum in the blue and red channels conforms to the common power-law shape after the absolute flux calibration.

Quasars usually show optical variabilities of 0.1–0.2 mag, which introduce additional uncertainties to the absolute flux calibration. However, the spectra without the absolute flux calibration information cannot be used to obtain important quantities such as continuum luminosity,  $M_{\text{BH}}$ , and emission-line flux. In previous papers of the LAMOST quasar survey (Papers I, II, and III), the spectra are not absolute flux calibrated, the continuum luminosity is inferred from the model fitting with the SDSS photometric data, and there is no emission-line

<sup>10</sup> The spectra of eight quasars that do not have reliable SDSS or Pan-STARRS1 photometric information are not flux-calibrated in this work.

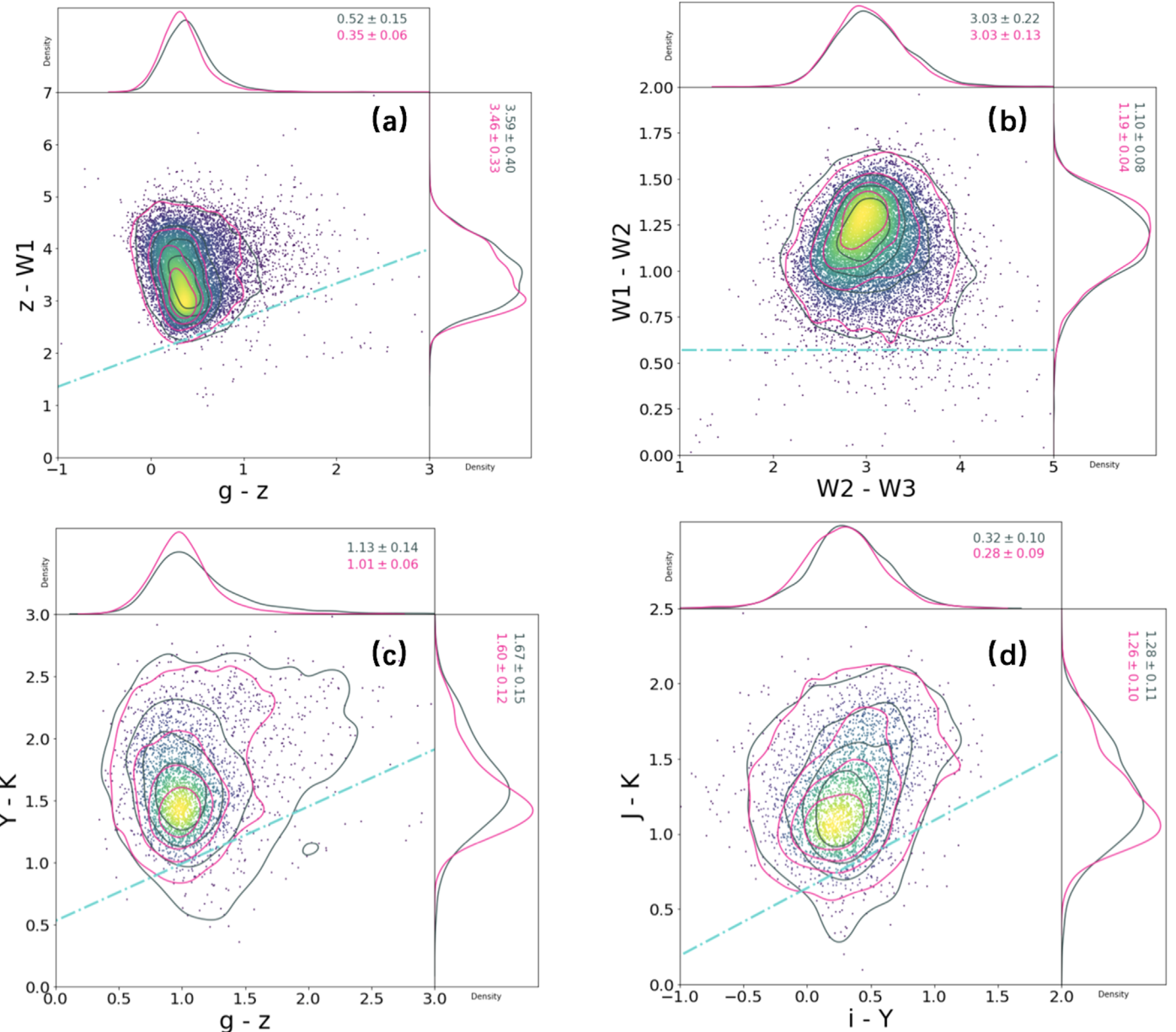


**Figure 3.** The distributions of identified LAMOST quasars in the SDSS-WISE/UKIDSS color diagram. The dashed-dotted lines indicate the criteria used in the LAMOST QSO survey (Wu & Jia 2010; Wu et al. 2012). The WISE and UKIDSS magnitudes are in Vega magnitudes. The SDSS magnitudes in panels (a) and (b) are plotted in AB magnitudes, and those in panels (c) and (d) are plotted in Vega magnitudes. The SDSS AB magnitudes can be converted to Vega magnitudes using the following scaling (Hewett et al. 2006):  $g = g(\text{AB}) + 0.103$ ,  $r = r(\text{AB}) - 0.146$ ,  $i = i(\text{AB}) - 0.366$ ,  $z = z(\text{AB}) - 0.533$ . The contours in pink show the distribution for common quasars between this work and SDSS, while the contours in gray show the distribution for unique quasars identified in this work. The mean ( $\mu$ ) and dispersion ( $\sigma$ ) of each distribution are tabulated in corresponding plots.

flux information in the published catalogs. Additionally, a small fraction of spectra ( $\sim 17\%$  in Paper II and  $\sim 6\%$  in Paper III) cannot be fitted properly owing to the connection defect near the overlapping region, which is solved by the absolute flux calibration in this work. Despite the uncertainties of our absolute flux calibration, it nevertheless helps us understand more about the central BHs of these quasars.

### 3.2. Spectral Fitting

Here we describe the fitting procedures for LAMOST quasar spectra. Before the fitting, each absolute-flux-calibrated spectrum is corrected for the Galactic extinction using the

reddening map (Schlegel et al. 1998) and the Milky Way extinction law of Fitzpatrick (1999) with  $R_V = 3.1$  and then transformed into the rest frame using the redshift obtained from the visual inspection.

Then, the spectra are fitted by the publicly available multicomponent spectral fitting code pyQSOFit (Guo et al. 2018) and a wrapper package based on it (QSOFITMORE; Fu 2021). The pyQSOFit performs the  $\chi^2$  fits, using the estimated errors per pixel that come from the reduction pipeline. A detailed description of the code and its application can be found in Guo et al. (2018), Shen et al. (2019), and Fu (2021).

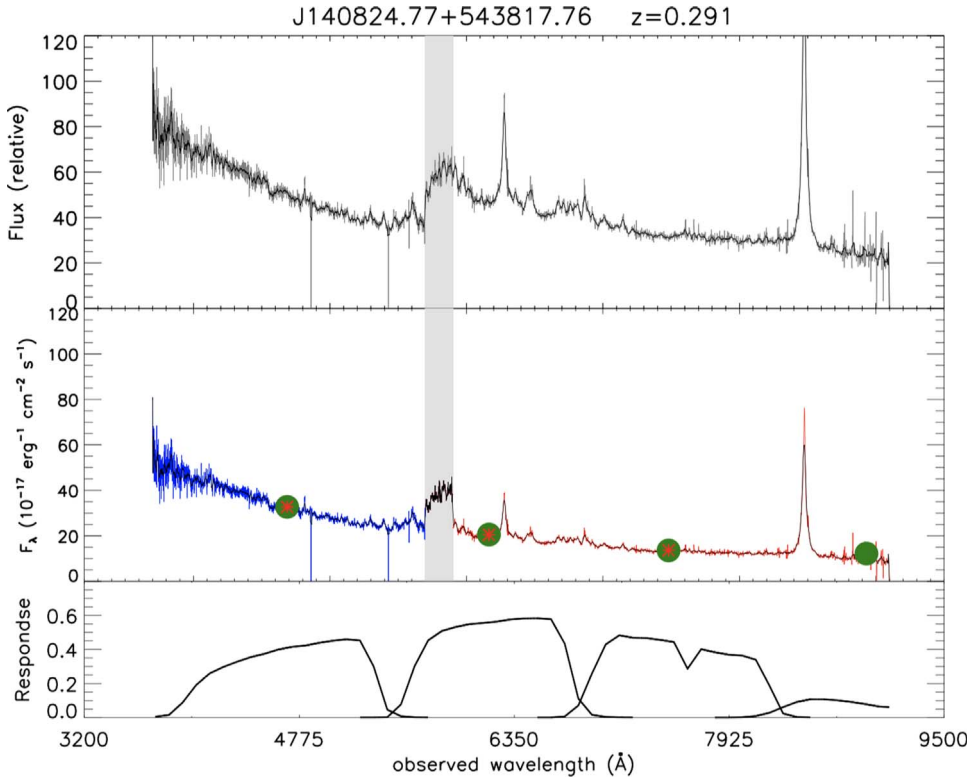


**Figure 4.** An example of absolute flux calibration for the blue- and red-arm LAMOST spectra. Top panel: the original spectrum only with the relative flux calibration. The gray area represents the blue/red overlapping region that is masked during the fitting. A connection defect can be observed at this region. Middle panel: the spectrum after the absolute flux calibration. The green circles represent the flux densities in the  $g$ ,  $r$ ,  $i$ , and  $z$  bands, and the asterisks mark the flux densities that are used during the fitting. The lines in blue and red represent piecewise fits to the asterisks. The connection defect is improved after recalibration. The bottom panel shows the filter curves for the SDSS in  $g$ ,  $r$ ,  $i$ , and  $z$  bands. It is clear that the  $z$  band is not fully covered by the spectrum, so the photometric data in  $z$  band are not used during the spectral fitting.

### 3.2.1. Continuum

The pseudocontinuum is fitted by a broken power law ( $f_{\text{bpl}}$ ) and a Fe II model ( $f_{\text{Fe II}}$ ) in the wavelength windows without quasar emission lines and outside the LAMOST spectral overlapping region. During the fitting, the turning point of the broken power law is fixed at 4661 Å at rest frame, which is similar to the value derived from the mean composite quasar spectra in Vanden Berk et al. (2001). Many works (Wills et al. 1985; Vanden Berk et al. 2001) show that there is an abrupt slope change near 5000 Å in the quasar continuum. One possible reason for the steeper slope at long wavelength is the near-infrared inflection, which is presumably caused by the emission from hot dust (Elvis et al. 1994). Another possible reason is the contamination from the host galaxies at low redshift. A trend of greater contribution from starlight with increasing wavelength is expected because the emission from host galaxies contributes a larger fraction at longer wavelength (Serote Roos et al. 1998; Vanden Berk et al. 2001). Both the external factors and a real change in the quasar continuum cause an abrupt change in its continuum slope (Vanden Berk et al. 2001). In the spectral fitting process, the iron model  $f_{\text{Fe II}}$

$$f_{\text{Fe II}} = b_0 F_{\text{Fe II}}(\lambda, b_1, b_2), \quad (1)$$

where the parameters  $b_0$ ,  $b_1$ ,  $b_2$  are the normalization, the FWHM of the Gaussian profile used to convolve the Fe II template, and the wavelength shift applied to the Fe II template, respectively. The optical Fe II template is based on Boroson & Green (1992). The UV Fe II template is a modified template

consisting of the templates in the wavelength range of 1000–2000 Å based on Vestergaard & Wilkes (2001), 2200–3090 Å based on Salviander et al. (2007), and 3090–3500 Å based on Tsuzuki et al. (2006). A few spectra have peculiar shapes in the continuum. This may be caused by some uncertainties in the SRC, which results from unstable efficiencies of some fibers and poor relative flux calibrations occasionally. It is difficult to find a suitable flux standard star for each spectrograph, especially for our extragalactic targets, as they are faint and located at high Galactic latitudes.

In this case, we add a three-order polynomial model ( $f_{\text{poly}}$ ) to solve this problem (Rakshit et al. 2020; Fu et al. 2022). Examples of the fitting results with (and without) the polynomial model are presented in Figure 5. When compared with SDSS spectra, it is clear that there is a peculiar shape in the continuum of LAMOST spectra (see the example in the bottom panel). Only a small fraction of objects require an additional polynomial component ( $\lesssim 0.3\%$ ). At last, the pseudocontinuum is fitted by two (or three) components:

$$f_{\text{cont}} = f_{\text{bpl}} + f_{\text{Fe II}} + (f_{\text{poly}}). \quad (2)$$

The host galaxy contamination is negligible for high- $z$  ( $z \gtrsim 0.5$ ) or high-luminosity ( $\log L_{5100} \gtrsim 44.5$ ) quasars. As for the  $z \lesssim 0.5$  low-luminosity quasars, the hosts on average can contribute  $\sim 15\%$  to the observed emissions and lead to a  $\sim 0.06$  dex overestimation of the 5100 Å continuum luminosity (Shen et al. 2011). However, due to the limitation of the spectral S/N for faint objects in our catalog, the process of host subtraction may bring larger uncertainties. Therefore, in this

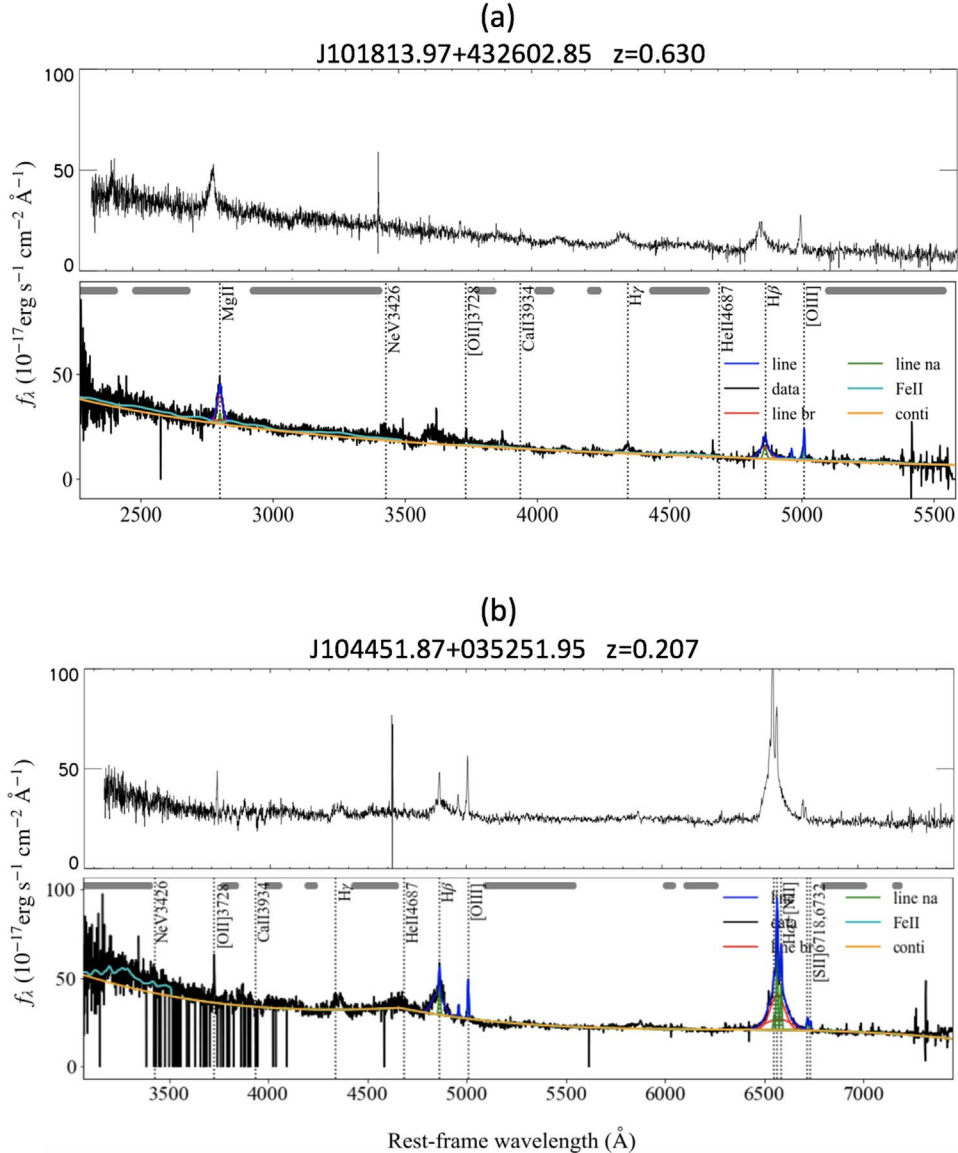


**Figure 5.** Two examples for the spectral fitting results with (panel (b)) and without (panel (a)) the polynomial model. In each pair of panels, the upper panel shows the spectrum from SDSS, and the lower panel shows the spectral fitting results of the LAMOST spectrum: the black lines denote the dereddened spectra, yellow lines represent the continuum model of ( $f_{\text{bpl}} + f_{\text{poly}}$ ), and the cyan lines represent Fe II templates. The details of emission-line components will be described in the later part.

work, the decomposition of the host galaxy is not applied to the spectra.

The fitted pseudocontinuum component is subtracted from the spectrum, and the remaining emission-line components are fitted with Gaussian profiles. We focus on four typical quasar emission lines: H $\alpha$ , H $\beta$ , Mg II, and C IV. They are the strongest broad emission lines in the available wavelength range and are commonly used as virial BH mass estimators. During the fitting, the parameters we mainly focus on are FWHM, equivalent width (EW), and flux. The fitting procedures for each line are described below.

### 3.2.2. H $\alpha$ Line

The pseudocontinuum-subtracted H $\alpha$ –[N II]–[S II] emission lines are fitted in the rest-frame windows [6350, 6800] Å for objects at  $z \lesssim 0.37$ . The broad component of H $\alpha$  is modeled by two Gaussian profiles, and the narrow components of H $\alpha$ , [N II]  $\lambda\lambda 6548, 6584$ , and [S II]  $\lambda\lambda 6716, 6731$  are each modeled

by a single Gaussian profile. The upper limit of FWHM for the narrow components is set to be 900 km s $^{-1}$ , which is a commonly used FWHM criterion to separate the narrow and broad lines (Wang et al. 2009; Coffey et al. 2019; Wang et al. 2019). The line widths and velocity offsets of the narrow lines are tied to each other. The relative flux ratio of the [N II]  $\lambda\lambda 6548, 6584$  doublet is fixed to 2.96. Examples of the best-fitting results of the H $\alpha$  line are given in Figure 6(a).

### 3.2.3. H $\beta$ Line

The pseudocontinuum-subtracted H $\beta$ –[O III] emission lines are fitted in the rest-frame window [4600, 5100] Å for objects at  $z \lesssim 0.8$ . Similar to H $\alpha$ , the broad component of H $\beta$  is modeled by two Gaussian profiles, and the narrow component of H $\beta$  is modeled by a single Gaussian profile. The upper limit of FWHM for the narrow components is set to be 900 km s $^{-1}$ . In addition to a single narrow component, the [O III]  $\lambda\lambda 4959, 5007$  double lines require blue wing components as has been

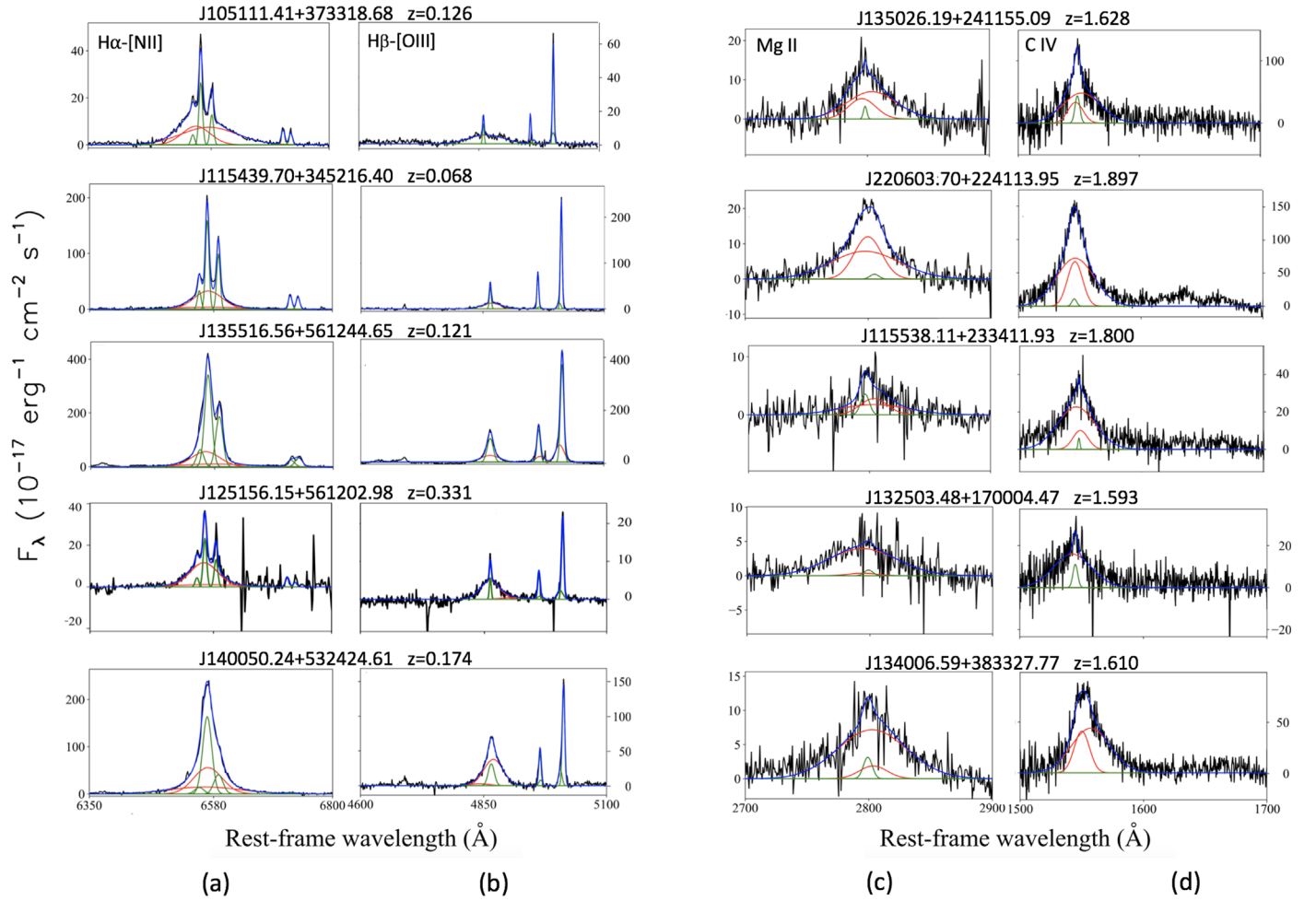


**Figure 6.** Examples for the deblending results of  $\text{H}\alpha$ -[N II]-[S II] (panel (a)),  $\text{H}\beta$ -[O III] (panel (b)), Mg II (panel (c)), and C IV (panel (d)) lines. The black lines represent the extinction-corrected spectra with the continuum subtracted. As for the fitted emission lines, the broad components are in red, while the narrow ones are in green, along with their sum (blue).

suggested by previous studies (e.g., Chadid et al. 2004; Boroson 2005; Komossa & Xu 2007; Zamfir et al. 2010; Schmidt et al. 2018). Therefore, each of the [O III]  $\lambda\lambda 4959, 5007$  double lines is modeled by two Gaussians, one for a line core and the other for the blueshifted wing, and neither of them is tied to the  $\text{H}\beta$  narrow component. The line widths and velocity offsets of the cores and wings are tied to each other. We constrain the relative flux ratio of [O III]  $\lambda\lambda 4959, 5007$  double lines to be the theoretical ratio of 1:3. Examples of the best-fitting results of the  $\text{H}\beta$  line are given in Figure 6(b).

#### 3.2.4. Mg II Line

Fittings of the Mg II and C IV emission lines are sometimes affected by the broad and narrow absorption features. In order to reduce the effect of narrow absorption features, we used the “`rej_abs = True`” option of the `QSOFITMORE` code when fitting Mg II and C IV emission lines. The code masks out the  $3\sigma$  outliers below the continuum model, which is useful to reduce the impact of absorption features (Shen et al. 2011; Shin et al. 2019).

We fit the Mg II emission line for objects at  $0.36 \lesssim z \lesssim 2.1$  in the rest-frame wavelength range of  $[2700, 2900]$  Å. The broad component of Mg II is modeled by two Gaussian profiles. As for the narrow component, the situation is more complicated. Some AGNs show the Mg II  $\lambda\lambda 2796, 2803$  double lines around

the peak, and the FWHM of each component is  $\lesssim 750$  km  $\text{s}^{-1}$  (Shen et al. 2011). However, such cases are rare, and most LAMOST spectra do not have adequate S/N and/or spectral resolution to separate these two components. Additionally, the narrow Mg II absorption line can lead to mimicking double peaks. Therefore, in this work we fit the Mg II narrow component with a single narrow Gaussian with an FWHM upper limit of 900 km  $\text{s}^{-1}$ . Examples of the best-fitting results of the Mg II line are given in Figure 6(c).

#### 3.2.5. C IV Line

We fit the C IV emission line for objects at  $1.5 \lesssim z \lesssim 4.4$  in the spectral rest-frame range of  $[1500, 1700]$  Å. Similar to other emission lines, the broad component of the C IV line is modeled by two Gaussian profiles. We do not set the upper limit for the FWHM of the narrow component because it is still debatable whether a strong narrow C IV component exists for most quasars (Assef et al. 2011; Denney 2012; Shen et al. 2019). In addition to the broad and narrow components, the parameters of the entire C IV profile are also given because (1) it is not certain whether the narrow component subtraction is feasible for the C IV emission line and (2) the existing C IV virial estimators are calculated with the FWHM from the entire C IV profiles. Examples of the best-fitting results of C IV are given in Figure 6(d).

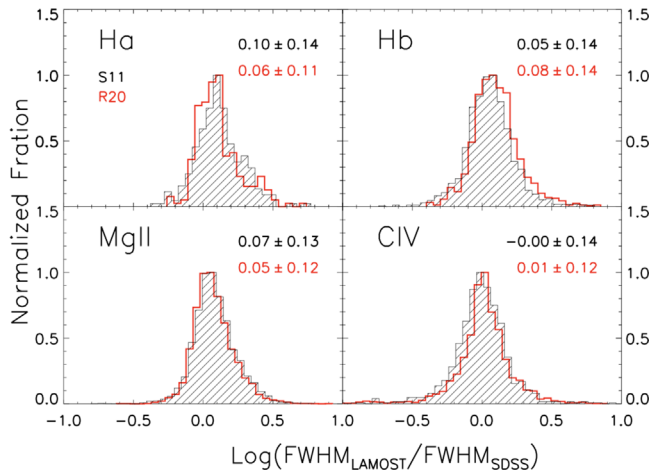


**Figure 7.** Comparisons between the measurements of the FWHM values in this work and S11 (R20). We show the plot of  $\log(\text{FWHM}_{\text{LAMOST}}/\text{FWHM}_{\text{SDSS}})$  for broad H $\alpha$  (top left), broad H $\beta$  (top right), broad Mg II (bottom left), and whole C IV (bottom right). The mean ( $\mu$ ) and dispersion ( $\sigma$ ) of each distribution are tabulated in corresponding plots. In this figure, only the emission lines with reliable fitting (LINE\_FLAG = 0) are considered.

### 3.2.6. The Reliability of the Spectral Fitting and Error Estimation

After the automatic fitting procedures, we visually inspect the fitting results for each object. The fittings are acceptable for most of the spectra with high S/N. The bad fittings are mainly caused by low S/N of the spectra and the lack of good pixels in the fitting region. A flag is given for each line based on the visual inspection: LINE\_FLAG = 0 indicates an acceptable fitting and reliable measurement; LINE\_FLAG = -1 indicates a spurious fitting; LINE\_FLAG = -9999 indicates that there are not enough good pixels in the fitting region owing to the limitation of spectral quality or wavelength region. The broad absorption line (BAL) features can also affect the fitting results. Those BAL features at Mg II and/or C IV are marked with BAL\_FLAG = 1.

There are 4964/6296 quasars in our catalog overlapping with the spectral fitting catalog of DR7Q/DR14Q (Shen et al. 2011, hereafter S11; Rakshit et al. 2020, hereafter R20). To further justify the fitting results in this work, we compare the measured parameters for the common quasars between LAMOST DR6–DR9 and S11 (R20). The histograms in Figure 7 compare the logarithm FWHM values. In general, we find excellent agreement between the measurements. The mean ( $\mu$ ) and standard deviation ( $\sigma$ ) of the difference between this work and S11 (R20) are  $0.10 \pm 0.14$  ( $0.06 \pm 0.11$ ) for H $\alpha$ ,  $0.05 \pm 0.14$  ( $0.08 \pm 0.14$ ) for H $\beta$ ,  $0.07 \pm 0.13$  ( $0.05 \pm 0.12$ ) for Mg II, and  $0.00 \pm 0.14$  ( $0.01 \pm 0.12$ ) for C IV lines. The EW values in these two catalogs are also in agreement with each other (Figure 8). The  $\mu$  and  $\sigma$  between this work and S11 (R20) are  $-0.10 \pm 0.14$  ( $-0.17 \pm 0.13$ ) for H $\alpha$ ,  $-0.10 \pm 0.22$  ( $-0.09 \pm 0.20$ ) for H $\beta$ ,  $0.00 \pm 0.17$  ( $-0.09 \pm 0.17$ ) for Mg II, and  $-0.05 \pm 0.21$  ( $-0.08 \pm 0.20$ ) for C IV lines. As mentioned before, there is no emission flux information in the previous papers of the LAMOST quasar survey. In Figure 9, we show the comparison of the emission-line flux measurements. The  $\mu$  and  $\sigma$  of the differences between this work and S11 (R20) are  $-0.15 \pm 0.13$  ( $-0.17 \pm 0.15$ ) for H $\alpha$ ,  $-0.09 \pm 0.18$  ( $-0.05 \pm 0.18$ ) for H $\beta$ ,  $0.04 \pm 0.17$  ( $-0.04 \pm 0.17$ ) for Mg II, and  $-0.03 \pm 0.18$  ( $-0.04 \pm 0.20$ ) for C IV lines. Similar to the

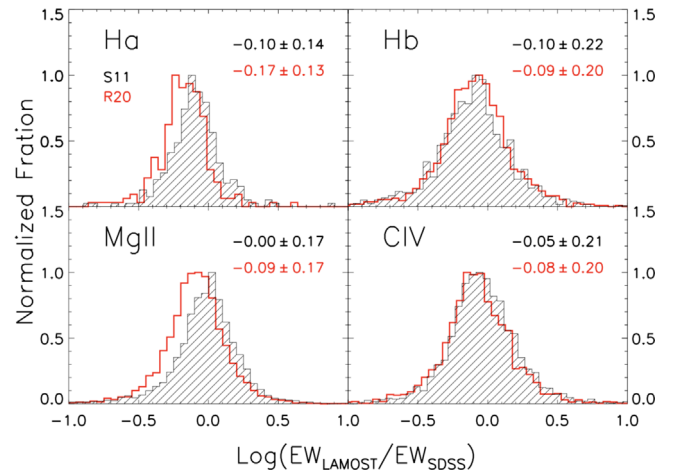


**Figure 8.** Same as in Figure 7, but for EW values.

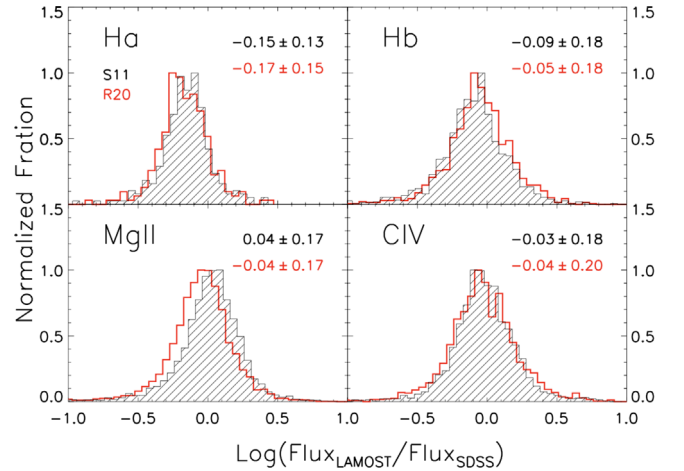


**Figure 9.** Same as in Figure 7, but for emission-line flux.

FWHM and EW, the emission fluxes also show excellent agreement between the different measurements.

In all cases, though a slight discrepancy between the different works is found, the measurements in this work are in agreement with those of SDSS. The differences may be caused by three main reasons: (1) Quasars usually show spectral variability, which can affect the measurements in different quasar catalogs. (2) The different S/N of SDSS and LAMOST spectra. As shown in Figure 10, the peaks of the median S/N per pixel in line-fitting regions are all around or below S/N = 5. Figure 11 shows the comparison of the median S/N per pixel of the line-fitting regions between LAMOST DR6–DR9 and S11 (R20). It is clear that the LAMOST spectra have significantly lower S/N than those of SDSS spectra. (3) The different model used in the spectral fitting. For example, in the continuum fitting process, the host galaxy subtraction is applied in R20, and there is an additional Balmer continuum component in the pseudocontinuum. The Fe II template (Vestergaard & Wilkes 2001) used in S11 is different from that in this work. There are also some differences in the emission-line-fitting process: we used the double Gaussians to model the broad component in H $\alpha$ , H $\beta$ , Mg II, and C IV emission lines, while in S11 or R20, multiple Gaussians (up to three) are used to fit each broad component. Moreover, in R20, there is no narrow component to model the C IV emission lines.

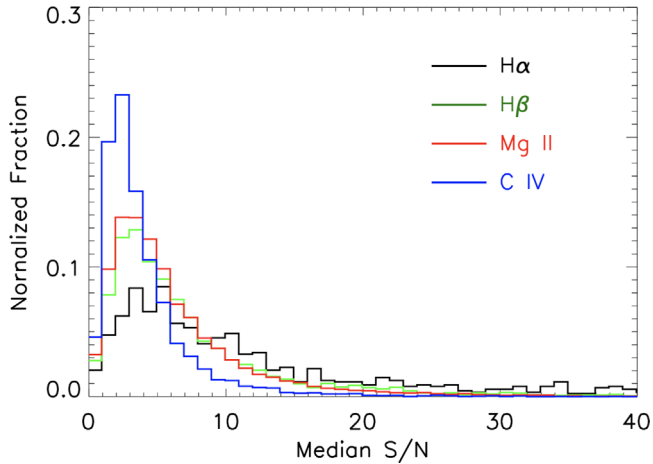


**Figure 10.** The distributions of median S/N per pixel around the line-fitting region are plotted as normalized histograms. Only the emission lines with reliable fitting (LINE\_FLAG = 0) are considered.

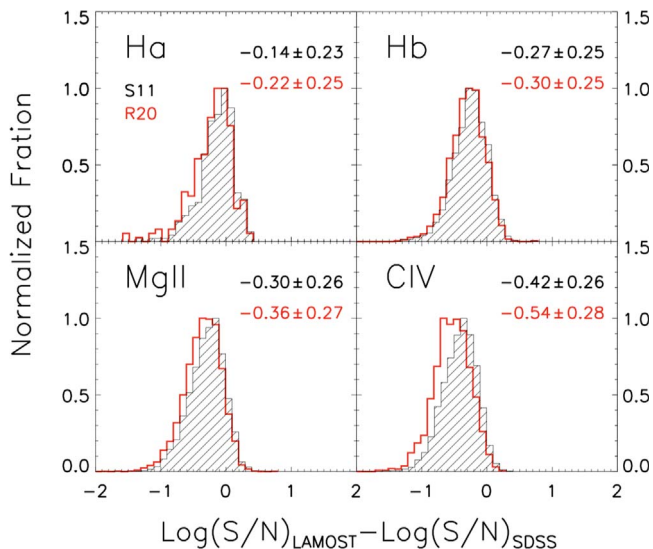


**Figure 11.** The comparison of the median S/N per pixel in the line-fitting region between this work and S11 (R20). The mean ( $\mu$ ) and dispersion ( $\sigma$ ) of each distribution are shown in corresponding plots. Only the emission lines with reliable fitting (LINE\_FLAG = 0) are considered.

The Monte Carlo (MC) approach is applied to estimate the uncertainty in each spectral fitting quantity. The mock spectrum is produced by adding a Gaussian random noise ( $N(0, \sigma^2)$ , where  $\sigma$  represents the uncertainty in the spectrum per pixel) to the original spectrum. Then, the spectral fitting is performed to the mock spectrum and the spectral quantities are estimated. The uncertainty of each quantity is then estimated as the standard deviation of the distribution given by 50 trials.

### 3.3. Virial Black Hole Mass

The monochromatic continuum luminosities at 1350 ( $L_{1350}$ ), 3000 ( $L_{3000}$ ), and 5100 ( $L_{5100}$ ) Å are calculated from the best-fit continuum ( $f_{\text{bpl}} + f_{\text{poly}}$ ). By assuming that the broad-line region (BLR) is virialized, the  $M_{\text{BH}}$  can be estimated based on the single-epoch spectrum. The monochromatic continuum luminosity is used as a proxy of the BLR radius, and the broad line width is used as a proxy of the virial velocity. The empirical scaling relation between the virial BH mass and these two

proxies is calibrated by AGN reverberation mapping. Here the H $\beta$ -based virial BH masses are estimated using the relation (Vestergaard & Peterson 2006)

$$\log M_{\text{BH}} = \log \left\{ \left[ \frac{\text{FWHM(H}\beta\text{)}}{\text{km s}^{-1}} \right]^2 \left[ \frac{L_{5100}}{10^{44} \text{ erg s}^{-1}} \right]^{0.5} \right\} + 0.91, \quad (3)$$

the Mg II-based virial BH masses are estimated using the relation (Wang et al. 2009)

$$\log M_{\text{BH}} = \log \left\{ \left[ \frac{\text{FWHM(MgII)}}{\text{km s}^{-1}} \right]^{1.51} \left[ \frac{L_{3000}}{10^{44} \text{ erg s}^{-1}} \right]^{0.5} \right\} + 2.60, \quad (4)$$

and the C IV-based virial BH masses are estimated using the relation (Vestergaard & Peterson 2006)

$$\log M_{\text{BH}} = \log \left\{ \left[ \frac{\text{FWHM(C IV)}}{\text{km s}^{-1}} \right]^2 \left[ \frac{L_{1350}}{10^{44} \text{ erg s}^{-1}} \right]^{0.53} \right\} + 0.66. \quad (5)$$

As mentioned before, the spectra are recalibrated using the photometric data observed at epochs that are different from those of the LAMOST observations, which will introduce additional uncertainties, because of the variations of quasar luminosity, generally with magnitudes of 0.1–0.2 mag. To justify this effect, we compare our continuum luminosities and  $M_{\text{BH}}$  measurements with those of S11 (R20) in Figure 12. In general, our estimates are in agreement with those of S11 (R20). The deviations between the continuum luminosity measurements in this work and those of SDSS are generally within 15%. If the variation of quasar luminosity is 0.1 (or 0.2) mag, the change of flux density estimated by the error transfer formula is  $\sim 9.2\%$  (or 18.4%). This means that the variation of quasar luminosity may dominate the error of the flux uncertainty for many quasars. Figure 13 shows the distribution of the  $M_{\text{BH}}$  at different redshifts. Most quasars observed in SDSS DR7Q have low to moderate redshifts, which is similar to the LAMOST survey, whereas in SDSS DR14Q, compared with SDSS DR7Q, there are a larger number of high-redshift and low-luminosity quasars observed. Therefore, it is apparent that the overall distribution of LAMOST quasars occupies a similar space to SDSS DR7Q but has a relatively large discrepancy from SDSS DR14Q. The comparisons in both Figures 12 and 13 prove that the flux recalibration is mostly valid and the  $M_{\text{BH}}$  given in this work can be considered as a good approximation.

## 4. Description of the Catalog

We provide a compiled catalog for the quasars identified in LAMOST DR6–DR9 along with this paper. All measured quantities will be tabulated in the online catalog at the LAMOST public website.<sup>11</sup> A summary of the parameters is listed in Table 2 and described below.

1. Unique spectra ID in LAMOST database.
2. Target observation date.

<sup>11</sup> <https://nadc.china-vo.org/?locale=en>

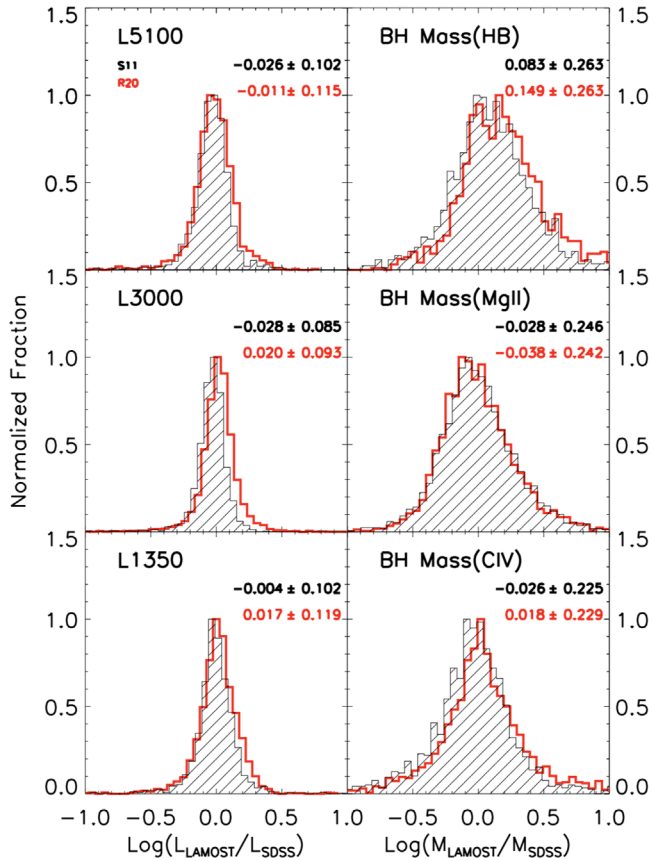


**Figure 12.** The comparison of the monochromatic continuum luminosities ( $L_{5100}$ ,  $L_{1000}$ ,  $L_{1300}$ ) and the estimated  $M_{\text{BH}}$  based on H $\beta$ , Mg II, and C IV between this work and S11 (R20).

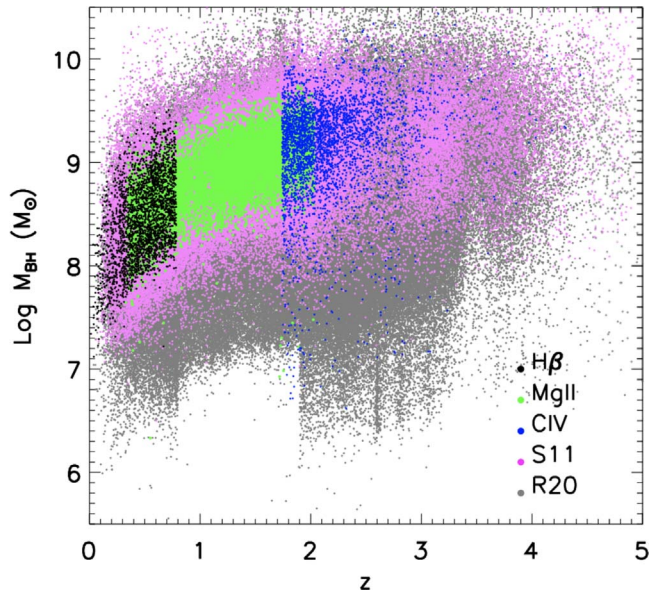


**Figure 13.** The distribution of  $M_{\text{BH}}$  based on various broad emissions (H $\beta$ , Mg II, and C IV) is plotted against the redshift. The quasars from S11 and R20 are represented by the pink and gray circles, respectively.

3. LAMOST object designation: Jhhmmss.ss + ddmmss.s (J2000).
4. R.A. and decl. (in decimal degrees, J2000).
5. Spectroscopic observation information: local modified Julian date (LMJD), spectroscopic plan name (PlanID),

- spectrograph identification (spID), and spectroscopic fiber number (fiberID). These four numbers are unique for each spectrum named in the format of spec–LMJD–planID\_spID–fiberID.fits.
6. Redshift and its flag (ZWARNING) based on visual inspections. 1 = not robust (e.g., only one emission line available).
  7. Target selection flag. SOURCE\_FLAG = “1” indicates that the quasar was selected by its infrared–optical color, data-mining algorithms, multiwavelength algorithms, or other serendipitous algorithms. SOURCE\_FLAG = “0” means that the object is not included in the LAMOST quasar survey candidate sample but identified as a quasar.
  8.  $M_i(z=2)$ : absolute  $i$ -band magnitude  $K$ -corrected to  $z=2$  following Richards et al. (2006).
  9. Number of spectroscopic observations for the quasar. When there is more than one observation for the object, the line properties are obtained from only one of the observations in which the S/N is highest.
  10. Median S/N per pixel in the continuum wavelength regions.
  11. Flag of broad absorption features. BAL\_FLAG = 1 indicates that broad absorption features are present in Mg II and/or C IV.
  12. FLUX, FWHM, rest-frame EW, and their uncertainties for broad H $\alpha$ , narrow H $\alpha$ , [N II]  $\lambda 6584$ , and [S II]  $\lambda\lambda 6716, 6731$  emission lines.
  13. Number of good pixels and median S/N per pixel for the spectrum in the H $\alpha$  region of rest-frame 6350–6800 Å.
  14. Flag indicates reliability of the emission-line-fitting results in the H $\alpha$  region upon visual inspections. 0 = acceptable; –1 = unacceptable. This value is set to be –9999 if H $\alpha$  is not measured owing to too few good pixels in the fitting region.
  15. FLUX, FWHM, rest-frame EW, and their uncertainties for broad H $\beta$ , narrow H $\beta$ , and [O III]  $\lambda 5007$  emission lines.
  16. Number of good pixels and median S/N per pixel for the spectrum in the H $\beta$  region of rest-frame 4600–5100 Å.
  17. Flag indicates reliability of the emission-line-fitting results in the H $\beta$  region upon visual inspections. 0 = acceptable; –1 = unacceptable. This value is set to be –9999 if H $\beta$  is not measured owing to too few good pixels in the fitting region.
  18. FLUX, FWHM, rest-frame EW, and their uncertainties for the broad and narrow Mg II emission line.
  19. Number of good pixels and median S/N per pixel for the spectrum in the Mg II region of rest-frame 2700–2900 Å.
  20. Flag indicates reliability of the emission-line-fitting results in the Mg II region upon visual inspections. 0 = acceptable; –1 = unacceptable. This value is set to be –9999 if Mg II is not measured owing to too few good pixels in the fitting region.
  21. FLUX, FWHM, rest-frame EW, and their uncertainties for the whole, broad, and narrow C IV emission line.
  22. Number of good pixels and median S/N per pixel for the spectrum in the C IV region of rest-frame 1500–1700 Å.
  23. Flag indicates reliability of the emission-line-fitting results in the C IV region upon visual inspections. 0 = acceptable; –1 = unacceptable. This value is set to be –9999 if C IV is not measured owing to too few good pixels in the fitting region.

**Table 2**  
Catalog Format for the Quasars Identified in LAMOST DR6–DR9

Column	Name	Format	Description
1	ObsID	LONG	Unique spectra ID in LAMOST database
2	ObsDate	STRING	Target observation date
3	NAME	STRING	LAMOST designation hhmmss.ss+ddmmss (J2000)
4	RA	DOUBLE	R.A. in decimal degrees (J2000)
5	DEC	DOUBLE	Decl. in decimal degrees (J2000)
6	LMJD	LONG	Local modified Julian day of observation
7	PLANID	STRING	Spectroscopic plan identification
8	SPID	LONG	Spectrograph identification
9	FIBERID	LONG	Spectroscopic fiber number
10	Z_VI	DOUBLE	Redshift based on visual inspection
11	ZWARNING	LONG	ZWARNING flag based on visual inspection
12	SOURCE_FLAG	LONG	Flag of quasar candidate selection
13	MI_Z2	DOUBLE	$M_i(z = 2)$ , $K$ -corrected to $z = 2$ following Richards et al. (2006)
14	NSPECOBS	LONG	Number of spectroscopic observations
15	SNR_SPEC	DOUBLE	Median S/N per pixel of the spectrum
16	BAL_FLAG	LONG	Flag of broad absorption features
17	FLUX_BROAD_HA	DOUBLE	Flux of broad H $\alpha$ in $10^{-17}$ erg cm $^{-2}$ s $^{-1}$
18	ERR_FLUX_BROAD_HA	DOUBLE	Uncertainty in FLUX <sub>H<math>\alpha</math>,broad</sub>
19	FWHM_BROAD_HA	DOUBLE	FWHM of broad H $\alpha$ in km s $^{-1}$
20	ERR_FWHM_BROAD_HA	DOUBLE	Uncertainty in FWHM <sub>H<math>\alpha</math>,broad</sub>
21	EW_BROAD_HA	DOUBLE	Rest-frame EW of broad H $\alpha$ in Å
22	ERR_EW_BROAD_HA	DOUBLE	Uncertainty in EW <sub>H<math>\alpha</math>,broad</sub>
23	FLUX_NARROW_HA	DOUBLE	Flux of narrow H $\alpha$ in $10^{-17}$ erg cm $^{-2}$ s $^{-1}$
24	ERR_FLUX_NARROW_HA	DOUBLE	Uncertainty in FLUX <sub>H<math>\alpha</math>,narrow</sub>
25	FWHM_NARROW_HA	DOUBLE	FWHM of narrow H $\alpha$ in km s $^{-1}$
26	ERR_FWHM_NARROW_HA	DOUBLE	Uncertainty in FWHM <sub>H<math>\alpha</math>,narrow</sub>
27	EW_NARROW_HA	DOUBLE	Rest-frame EW of narrow H $\alpha$ in Å
28	ERR_EW_NARROW_HA	DOUBLE	Uncertainty in EW <sub>H<math>\alpha</math>,narrow</sub>
29	FLUX_NII_6584	DOUBLE	Flux of [N II] $\lambda\lambda 6584$ in $10^{-17}$ erg cm $^{-2}$ s $^{-1}$
30	ERR_FLUX_NII_6584	DOUBLE	Uncertainty in FLUX <sub>[N II]6584</sub>
31	FWHM_NII_6584	DOUBLE	FWHM of [N II] $\lambda\lambda 6584$ in km s $^{-1}$
32	ERR_FWHM_NII_6584	DOUBLE	Uncertainty in FWHM <sub>[N II]6584</sub>
33	EW_NII_6584	DOUBLE	Rest-frame EW of [N II] $\lambda\lambda 6584$ in Å
34	ERR_EW_NII_6584	DOUBLE	Uncertainty in EW <sub>[N II]6584</sub>
35	FLUX_SII_6716	DOUBLE	Flux of [S II] $\lambda\lambda 6716$ in $10^{-17}$ erg cm $^{-2}$ s $^{-1}$
36	ERR_FLUX_SII_6716	DOUBLE	Uncertainty in FLUX <sub>[S II]6716</sub>
37	FWHM_SII_6716	DOUBLE	FWHM of [S II] $\lambda\lambda 6716$ in km s $^{-1}$
38	ERR_FWHM_SII_6716	DOUBLE	Uncertainty in FWHM <sub>[S II]6716</sub>
39	EW_SII_6716	DOUBLE	Rest-frame EW of [S II] $\lambda\lambda 6716$ in Å
40	ERR_EW_SII_6716	DOUBLE	Uncertainty in EW <sub>[S II]6716</sub>
41	FLUX_SII_6731	DOUBLE	Flux of [S II] $\lambda\lambda 6731$ in $10^{-17}$ erg cm $^{-2}$ s $^{-1}$
42	ERR_FLUX_SII_6731	DOUBLE	Uncertainty in FLUX <sub>[S II]6731</sub>
43	FWHM_SII_6731	DOUBLE	FWHM of [S II] $\lambda\lambda 6731$ in km s $^{-1}$
44	ERR_FWHM_SII_6731	DOUBLE	Uncertainty in FWHM <sub>[S II]6731</sub>
45	EW_SII_6731	DOUBLE	Rest-frame EW of [S II] $\lambda\lambda 6731$ in Å
46	ERR_EW_SII_6731	DOUBLE	Uncertainty in EW <sub>[S II]6731</sub>
47	LINE_NPIX_HA	LONG	Number of good pixels for the rest-frame 6350–6800 Å
48	LINE_MED_SN_HA	DOUBLE	Median S/N per pixel for the rest-frame 6350–6800 Å
49	LINE_FLAG_HA	LONG	Flag for the quality in H $\alpha$ fitting
50	FLUX_BROAD_HB	DOUBLE	Flux of broad H $\beta$ in $10^{-17}$ erg cm $^{-2}$ s $^{-1}$
51	ERR_FLUX_BROAD_HB	DOUBLE	Uncertainty in FLUX <sub>H<math>\beta</math>,broad</sub>
52	FWHM_BROAD_HB	DOUBLE	FWHM of broad H $\beta$ in km s $^{-1}$
53	ERR_FWHM_BROAD_HB	DOUBLE	Uncertainty in FWHM <sub>H<math>\beta</math>,broad</sub>
54	EW_BROAD_HB	DOUBLE	Rest-frame EW of broad H $\beta$ in Å
55	ERR_EW_BROAD_HB	DOUBLE	Uncertainty in EW <sub>H<math>\beta</math>,broad</sub>
56	FLUX_NARROW_HB	DOUBLE	Flux of narrow H $\beta$ in $10^{-17}$ erg cm $^{-2}$ s $^{-1}$
57	ERR_FLUX_NARROW_HB	DOUBLE	Uncertainty in FLUX <sub>H<math>\beta</math>,narrow</sub>
58	FWHM_NARROW_HB	DOUBLE	FWHM of narrow H $\beta$ in km s $^{-1}$
59	ERR_FWHM_NARROW_HB	DOUBLE	Uncertainty in FWHM <sub>H<math>\beta</math>,narrow</sub>
60	EW_NARROW_HB	DOUBLE	Rest-frame EW of narrow H $\beta$ in Å
61	ERR_EW_NARROW_HB	DOUBLE	Uncertainty in EW <sub>H<math>\beta</math>,narrow</sub>
62	FLUX_OIII_5007	DOUBLE	Flux of [O III] $\lambda\lambda 5007$ in $10^{-17}$ erg cm $^{-2}$ s $^{-1}$

**Table 2**  
(Continued)

Column	Name	Format	Description
63	ERR_FLUX_OIII_5007	DOUBLE	Uncertainty in $\text{FLUX}_{\text{OIII}5007}$
64	FWHM_OIII_5007	DOUBLE	$\text{FWHM of } [\text{O III}] \lambda 5007 \text{ in km s}^{-1}$
65	ERR_FWHM_OIII_5007	DOUBLE	Uncertainty in $\text{FWHM}_{\text{OIII}5007}$
66	EW_OIII_5007	DOUBLE	Rest-frame EW of $[\text{O III}] \lambda 5007 \text{ in } \text{\AA}$
67	ERR_EW_OIII_5007	DOUBLE	Uncertainty in $\text{EW}_{\text{OIII}5007}$
68	LINE_NPIX_HB	LONG	Number of good pixels for the rest-frame 4600–5100 $\text{\AA}$
69	LINE_MED_SN_HB	DOUBLE	Median S/N per pixel for the rest-frame 4600–5100 $\text{\AA}$
70	LINE_FLAG_HB	LONG	Flag for the quality in $\text{H}\beta$ fitting
71	FLUX_BROAD_MGII	DOUBLE	Flux of the broad Mg II in $10^{-17} \text{ erg cm}^{-2} \text{ s}^{-1}$
72	ERR_FLUX_BROAD_MGII	DOUBLE	Uncertainty in $\text{FLUX}_{\text{MgII},\text{broad}}$
73	FWHM_BROAD_MGII	DOUBLE	$\text{FWHM of the broad Mg II in km s}^{-1}$
74	ERR_FWHM_BROAD_MGII	DOUBLE	Uncertainty in $\text{FWHM}_{\text{MgII},\text{broad}}$
75	EW_BROAD_MGII	DOUBLE	Rest-frame EW of the broad Mg II in $\text{\AA}$
76	ERR_EW_BROAD_MGII	DOUBLE	Uncertainty in $\text{EW}_{\text{MgII},\text{broad}}$
77	FLUX_NARROW_MGII	DOUBLE	Flux of the narrow Mg II in $10^{-17} \text{ erg cm}^{-2} \text{ s}^{-1}$
78	ERR_FLUX_NARROW_MGII	DOUBLE	Uncertainty in $\text{FLUX}_{\text{MgII},\text{narrow}}$
79	FWHM_NARROW_MGII	DOUBLE	$\text{FWHM of the narrow Mg II in km s}^{-1}$
80	ERR_FWHM_NARROW_MGII	DOUBLE	Uncertainty in $\text{FWHM}_{\text{MgII},\text{narrow}}$
81	EW_NARROW_MGII	DOUBLE	Rest-frame EW of the narrow Mg II in $\text{\AA}$
82	ERR_EW_NARROW_MGII	DOUBLE	Uncertainty in $\text{EW}_{\text{MgII},\text{narrow}}$
83	LINE_NPIX_MGII	LONG	Number of good pixels for the rest-frame 2700–2900 $\text{\AA}$
84	LINE_MED_SN_MGII	DOUBLE	Median S/N per pixel for the rest-frame 2700–2900 $\text{\AA}$
85	LINE_FLAG_MGII	LONG	Flag for the quality in Mg II fitting
86	FLUX_CIV	DOUBLE	Flux of the whole C IV in $10^{-17} \text{ erg cm}^{-2} \text{ s}^{-1}$
87	ERR_FLUX_CIV	DOUBLE	Uncertainty in $\text{Flux}_{\text{CIV},\text{whole}}$
88	FWHM_CIV	DOUBLE	$\text{FWHM of the whole C IV in km s}^{-1}$
89	ERR_FWHM_CIV	DOUBLE	Uncertainty in $\text{FWHM}_{\text{CIV},\text{whole}}$
90	EW_CIV	DOUBLE	Rest-frame EW of the whole C IV in $\text{\AA}$
91	ERR_EW_CIV	DOUBLE	Uncertainty in $\text{EW}_{\text{CIV},\text{whole}}$
92	FLUX_BROAD_CIV	DOUBLE	Flux of the broad C IV in $10^{-17} \text{ erg cm}^{-2} \text{ s}^{-1}$
93	ERR_FLUX_BROAD_CIV	DOUBLE	Uncertainty in $\text{Flux}_{\text{CIV},\text{broad}}$
94	FWHM_BROAD_CIV	DOUBLE	$\text{FWHM of the broad C IV in km s}^{-1}$
95	ERR_FWHM_BROAD_CIV	DOUBLE	Uncertainty in $\text{FWHM}_{\text{CIV},\text{broad}}$
96	EW_BROAD_CIV	DOUBLE	Rest-frame EW of the broad C IV in $\text{\AA}$
97	ERR_EW_BROAD_CIV	DOUBLE	Uncertainty in $\text{EW}_{\text{CIV},\text{broad}}$
98	FLUX_NARROW_CIV	DOUBLE	Flux of the narrow C IV in $10^{-17} \text{ erg cm}^{-2} \text{ s}^{-1}$
99	ERR_FLUX_NARROW_CIV	DOUBLE	Uncertainty in $\text{Flux}_{\text{CIV},\text{narrow}}$
100	FWHM_NARROW_CIV	DOUBLE	$\text{FWHM of the narrow C IV in km s}^{-1}$
101	ERR_FWHM_NARROW_CIV	DOUBLE	Uncertainty in $\text{FWHM}_{\text{CIV},\text{narrow}}$
102	EW_NARROW_CIV	DOUBLE	Rest-frame EW of the narrow C IV in $\text{\AA}$
103	ERR_EW_NARROW_CIV	DOUBLE	Uncertainty in $\text{EW}_{\text{CIV},\text{narrow}}$
104	LINE_NPIX_CIV	LONG	Number of good pixels for the rest-frame 1500–1700 $\text{\AA}$
105	LINE_MED_SN_CIV	DOUBLE	Median S/N per pixel for the rest-frame 1500–1700 $\text{\AA}$
106	LINE_FLAG_CIV	LONG	Flag for the quality in C IV fitting
107	ALPHA_LAMBDA_1	DOUBLE	Wavelength power-law index from blueward of 4661 $\text{\AA}$
108	ALPHA_LAMBDA_2	DOUBLE	Wavelength power-law index from redward of 4661 $\text{\AA}$
109	Fe_op_norm	DOUBLE	The normalization applied to the optical Fe II template
110	Fe_op_shift	DOUBLE	The Gaussian FWHM applied to the optical Fe II template
111	Fe_op_FWHM	DOUBLE	The wavelength shift applied to the optical Fe II template
112	Fe_uv_norm	DOUBLE	The normalization applied to the ultraviolet Fe II template
113	Fe_uv_shift	DOUBLE	The Gaussian FWHM applied to the ultraviolet Fe II template
114	Fe_uv_FWHM	DOUBLE	The wavelength shift applied to the ultraviolet Fe II template
115	LOGL1350	DOUBLE	Monochromatic luminosity at 1350 $\text{\AA}$ in $\text{erg s}^{-1}$
116	ERR_LOGL1350	DOUBLE	Uncertainty in $\log L_{1350}$
117	LOGL3000	DOUBLE	Monochromatic luminosity at 3000 $\text{\AA}$ in $\text{erg s}^{-1}$
118	ERR_LOGL3000	DOUBLE	Uncertainty in $\log L_{3000}$
119	LOGL5100	DOUBLE	Monochromatic luminosity at 5100 $\text{\AA}$ in $\text{erg s}^{-1}$
120	ERR_LOGL5100	DOUBLE	Uncertainty in $\log L_{5100}$
121	LOGBH_HB	DOUBLE	Virial BH mass ( $M_\odot$ ) based on $\text{H}\beta$
122	LOGBH_MgII	DOUBLE	Virial BH mass ( $M_\odot$ ) based on Mg II
123	LOGBH_CIV	DOUBLE	Virial BH mass ( $M_\odot$ ) based on C IV

**Table 2**  
(Continued)

Column	Name	Format	Description
124	SDSS_NAME	STRING	Name of the quasar in the SDSS quasar catalog
125	2RXS_NAME	STRING	Name of the object in the second ROSAT all-sky survey point-source catalog
126	2RXS_CTS	DOUBLE	Background-corrected source counts in 0.1–2.4 keV from 2RXS source catalog
127	2RXS_ECTS	DOUBLE	Error of the source counts from 2RXS source catalog
128	2RXS_EXPTIME	DOUBLE	Source exposure time from 2RXS source catalog
129	LM_2RXS_SEP	DOUBLE	LAMOST–2RXS separation in arcsec
130	4XMM_NAME	STRING	Name of the object in XMM-Newton Serendipitous Source Catalog
131	4XMM_FLUX	DOUBLE	Flux in 0.2–12.0 keV band from 4XMM-DR11 (in $\text{erg s}^{-1} \text{cm}^{-2}$ )
132	4XMM_FLUX_ERR	DOUBLE	Error of the flux in 0.2–12.0 keV band from 4XMM-DR11 (in $\text{erg s}^{-1} \text{cm}^{-2}$ )
133	LM_4XMM_SEP	DOUBLE	LAMOST–4XMM separation in arcseconds
134	FPEAK	DOUBLE	FIRST peak flux density at 20 cm in mJy
135	LM_FIRST_SEP	DOUBLE	LAMOST–FIRST separation in arcseconds
136	g_mag	DOUBLE	SDSS (or Pan-STARRS1 PSF) <i>g</i> magnitudes
137	ERR_g_mag	DOUBLE	<i>g</i> PSF magnitude errors
138	r_mag	DOUBLE	SDSS (or Pan-STARRS1) <i>r</i> PSF magnitudes
139	ERR_r_mag	DOUBLE	<i>r</i> PSF magnitude errors
140	i_mag	DOUBLE	SDSS (or Pan-STARRS1) <i>i</i> PSF magnitudes
141	ERR_i_mag	DOUBLE	<i>i</i> PSF magnitude errors
142	z_mag	DOUBLE	SDSS (or Pan-STARRS1) <i>z</i> PSF magnitudes
143	ERR_z_mag	DOUBLE	<i>z</i> PSF magnitude errors
144	MAG_FLAG	LONG	Flag of PSF magnitude
145	W1_mag	DOUBLE	Instrumental profile-fit photometry magnitudes, W1 band
146	ERR_W1_mag	DOUBLE	W1 magnitude errors
147	W2_mag	DOUBLE	Instrumental profile-fit photometry magnitudes, W2 band
148	ERR_W2_mag	DOUBLE	W2 magnitude errors
149	W3_mag	DOUBLE	Instrumental profile-fit photometry magnitudes, W3 band
150	ERR_W3_mag	DOUBLE	W3 magnitude errors
151	Y_mag	DOUBLE	<i>Y</i> AperMag3 magnitudes (2" aperture diameter)
152	ERR_Y_mag	DOUBLE	<i>Y</i> magnitude errors
153	J_mag	DOUBLE	<i>J</i> AperMag3 magnitudes (2" aperture diameter)
154	ERR_J_mag	DOUBLE	<i>J</i> magnitude errors
155	K_mag	DOUBLE	<i>K</i> AperMag3 magnitudes (2" aperture diameter)
156	ERR_K_mag	DOUBLE	<i>K</i> magnitude errors

(This table is available in its entirety in FITS format.)

**Table 3**  
The Summary of the Results of the LAMOST Quasar Survey up to Now

	Paper I	Paper II	Paper III	This Work	Total
Total	3921	19,935	19,253	13,066	56,175
Known	2741	11,835	11,091	6381	32,048
Independent	1180	12,126	11,458	7102	31,866
New	1180	8100	8162	6685	24,127

24. Wavelength power-law index,  $\alpha_\lambda$ , from blueward of 4661 Å.
25. Wavelength power-law index,  $\alpha_\lambda$ , from redward of 4661 Å.
26. Rest-frame normalization parameter of optical Fe II.
27. Rest-frame Gaussian FWHM of optical Fe II complex.
28. Rest-frame wavelength shift of optical Fe II complex.
29. Rest-frame normalization parameter of UV Fe II complex.
30. Rest-frame Gaussian FWHM of UV Fe II complex.
31. Rest-frame wavelength shift of UV Fe II complex.
32. Monochromatic luminosities and their uncertainties at 1350, 3000, and 5100 Å.
33. Virial BH masses (in  $M_\odot$ ) with calibrations of Hβ, Mg II, and C IV.

34. Name of the quasar in the SDSS quasar catalog. The LAMOST DR6–DR9 quasar catalog was cross-correlated with the SDSS quasar catalog (DR14; Pâris et al. 2018) using a matching radius of 3".
35. Name of the object in the second ROSAT all-sky survey point-source catalog (2RXS; Boller et al. 2016). The LAMOST DR6–DR9 quasar catalog was cross-correlated with 2RXS using a matching radius of 30". The nearest point source in 2RXS was chosen.
36. The background-corrected source counts in full band (0.1–2.4 keV), and its error, from 2RXS.
37. The exposure time of the ROSAT measurement.
38. Angular separation between the LAMOST and 2RXS source positions.
39. Name of the object in the XMM-Newton Serendipitous Source Catalog. The LAMOST DR6–DR9 quasar catalog was cross-correlated with the XMM-Newton Serendipitous Source Catalog (4XMM-DR11; Webb et al. 2020) using a matching radius of 3".
40. The mean full-band (0.2–12 keV) flux, and its error, from 4XMM-DR11.
41. Angular separation between the LAMOST and 4XMM-DR11 source positions.

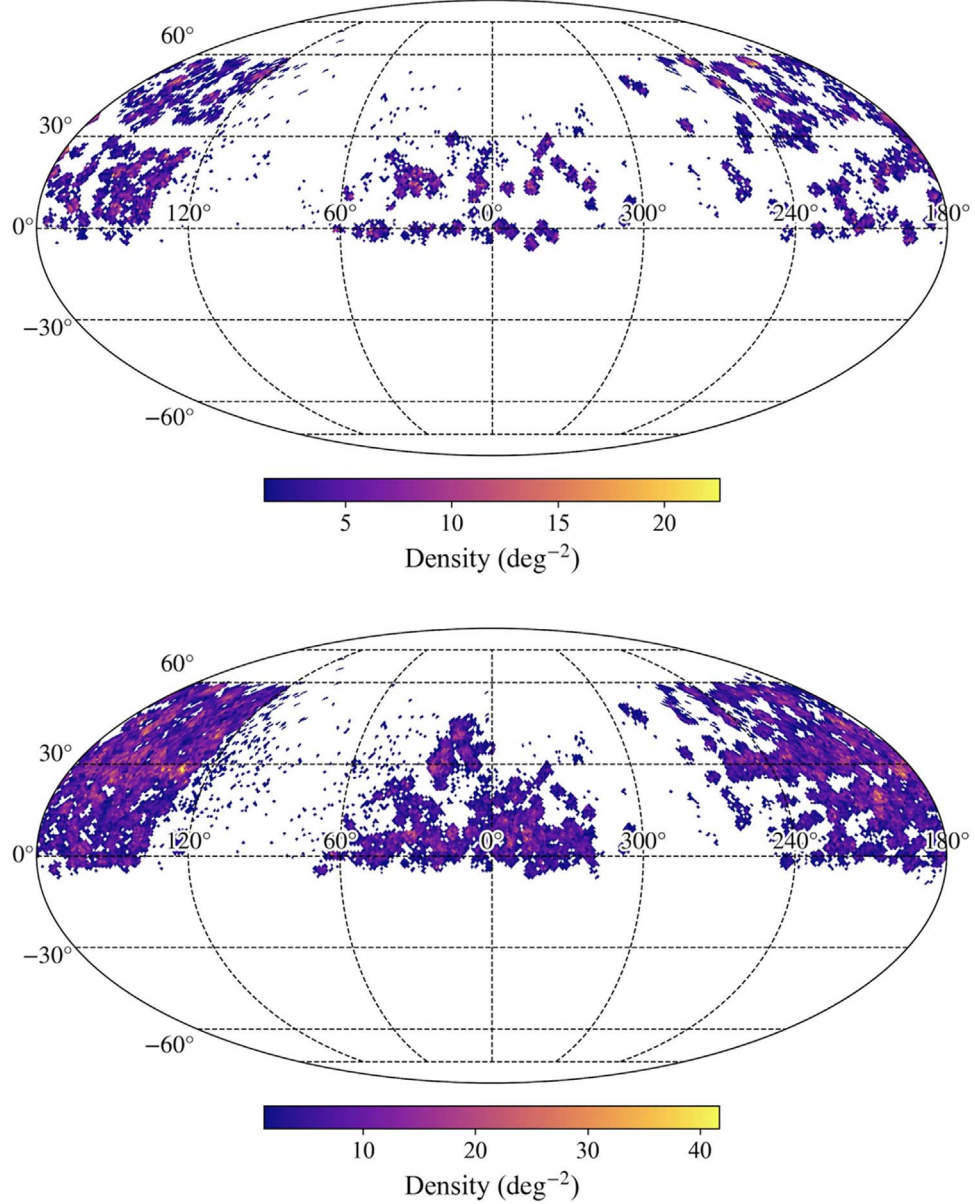


**Figure 14.** The HEALPix sky distributions of the quasars identified in LAMOST DR6–DR9 (panel (a)) and DR1–DR9 (panel (b)) are shown in equatorial coordinates with the parameters  $N_{\text{side}} = 64$  and area of  $0.839 \text{ deg}^2$  per pixel.

- 42. FIRST peak flux density at 20 cm in units of mJy. The LAMOST DR6–DR9 quasar catalog was cross-correlated with the FIRST survey catalog using a matching radius of 5''.
- 43. Angular separation between LAMOST and FIRST source positions.
- 44. SDSS (or Pan-STARRS1)  $g$ ,  $r$ ,  $i$ ,  $z$  PSF magnitudes without the correction for Galactic extinction, and their uncertainties.
- 45. Flag of PSF magnitudes. “MAG\_FLAG = 1” indicates that the PSF magnitudes are given by SDSS, “MAG\_FLAG = 0” indicates that the PSF magnitudes are given by Pan-STARRS1, and “MAG\_FLAG = -1” indicates that the quasars do not have reliable photometric information.
- 46. WISE W1, W2, W3 instrumental profile-fit photometry magnitudes without the correction for Galactic extinction, and their uncertainties.
- 47. WISE  $Y$ ,  $J$ ,  $K$  AperMag3 magnitudes without the correction for Galactic extinction, and their uncertainties. The AperMag3 magnitudes are the aperture-corrected magnitudes measured by UKIDSS with 2'' diameter, providing the most accurate estimate of the total magnitude (Dye et al. 2006).

## 5. Summary and Discussion

In this work, we present the result of the LAMOST quasar survey in the sixth, seventh, eighth, and ninth data releases. There are in total 13,066 visually confirmed quasars. Among the identified quasars, 6381 were reported by the SDSS DR14 quasar catalog after our survey began, while the remaining 6685 are considered as newly discovered.

We applied the emission-line measurements of H $\alpha$ , H $\beta$ , Mg II, and C IV for each confirmed quasar. As the LAMOST

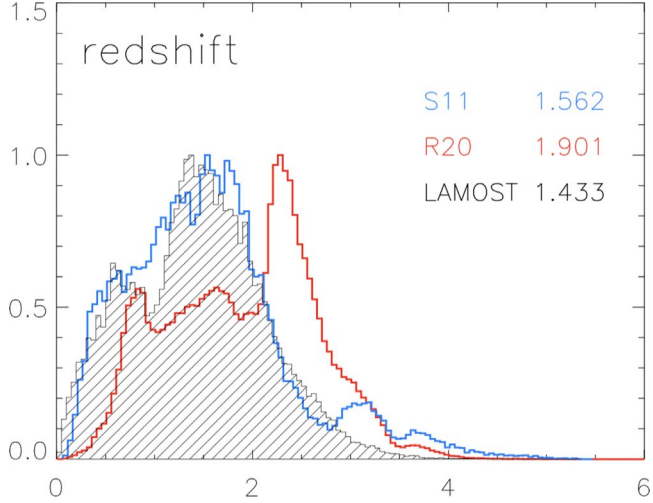


**Figure 15.** The redshift distributions of LAMOST (black) and SDSS (blue for S11, and red for R20) samples. The mean redshifts are tabulated in the upper right corner.

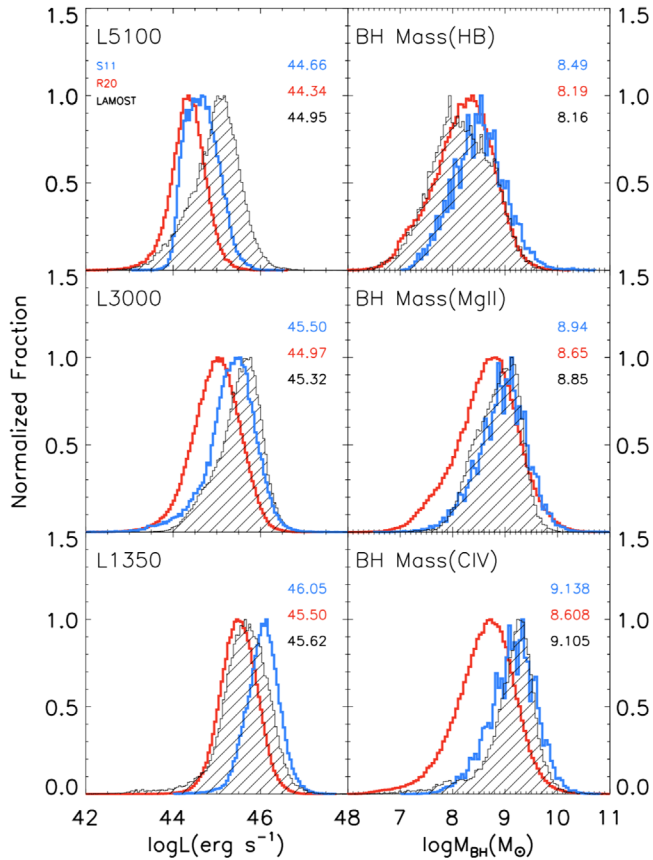


**Figure 16.** The histograms of the monochromatic continuum luminosities ( $L_{5100}$ ,  $L_{1000}$ ,  $L_{1300}$ ) and the estimated  $M_{\text{BH}}$  (based on H $\beta$ , Mg II, and C IV) for the LAMOST and S11 (R20) quasar sample. The mean value of each distribution is tabulated in the upper right corner.

spectra lack information of absolute flux calibration, we recalibrate the spectra by fitting the SDSS/Pan-STARRS1 photometric data. The measured quantities are compiled into the quasar catalog, which is available online.

After the 9 yr regular survey (Ai et al. 2016; Dong et al. 2018; Yao et al. 2019, and this work), there are in total 56,175 identified quasars in the LAMOST quasar survey, of which

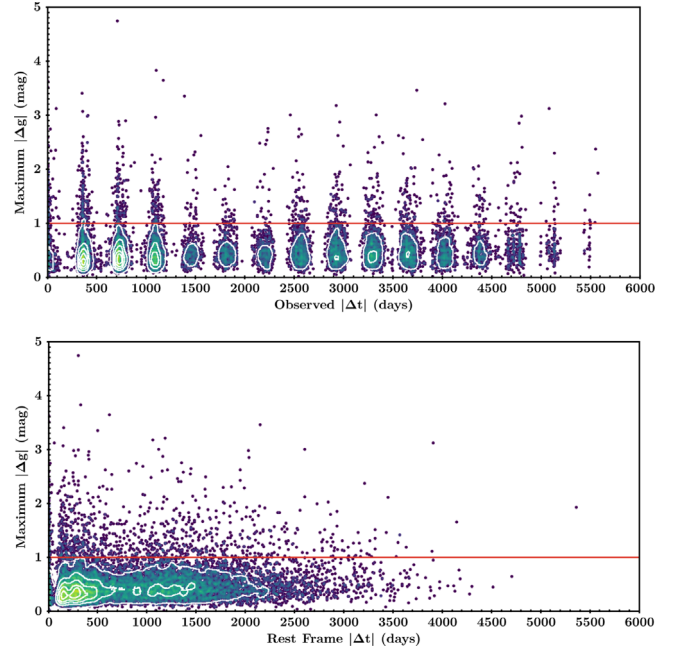


**Figure 17.** Top panel: the distribution of the maximum magnitude difference based on SDSS and PS1 photometry  $|\Delta g|$  vs. time lag  $\Delta t$ . Bottom panel: the same distribution as in the top panel, but the observed-frame lag is switching to the rest-frame lag by dividing  $(1 + z)$ .

31,866 are independently discovered by LAMOST. Among the identified quasars, 24,127 are newly discovered, and the remaining 32,048 are known ones that are reported by SDSS or Milliquas (see Table 3). The sky distribution of LAMOST identified quasars is shown in Figure 14.

The basic properties of quasars identified in LAMOST DR1–DR9 are compared with SDSS quasars. Figure 15 presents the redshift distribution of quasars for each sample. Generally, the redshift of the LAMOST sample is slightly lower than that of S11 and R20, but it is overall much more similar to S11, being only 0.13 smaller in the mean value. The distributions of  $M_{\text{BH}}$  and continuum luminosities ( $L_{5100}$ ,  $L_{1000}$ , and  $L_{1300}$ ) of LAMOST quasars are also compared with those of S11 and R20 in Figure 16. As for the continuum luminosities of the LAMOST sample,  $L_{5100}$  is higher than those of S11 and R20,  $L_{1000}$  is similar to those of S11, while  $L_{1300}$  is similar to those of R20. The distribution of H $\beta$ -based  $M_{\text{BH}}$  in the LAMOST sample is similar to R20, while the Mg II- and C IV-based  $M_{\text{BH}}$  in the LAMOST sample are similar to S11. These distributions indicate that the quasars from the LAMOST survey are brighter and have lower  $M_{\text{BH}}$  at lower redshift when compared with quasars from SDSS.

The optical variability of LAMOST quasars can be quantified by the maximum photometric difference between the  $g$ -band magnitude of SDSS and Pan-STARRS1 ( $|\Delta g|_{\text{max}}$ ). To avoid the significant contamination from the poor photometry, we reject the photometric data with uncertainties  $\sigma_g \geq 0.15$  mag. Figure 17 shows the distribution of  $|\Delta g|_{\text{max}}$  versus time lag  $|\Delta t|$  with contours. The photometric variability of most quasars is within 1 mag, while some of them have at least a 1.0 mag change in their  $g$ -band light curves. Some previous works (MacLeod et al. 2016; Yang et al. 2018) showed that the photometry varies following the spectral type transition, and the criterion  $|\Delta g|_{\text{max}} > 1.0$  was used to select CL-AGNs candidates. Some examples of CL-AGNs discovered

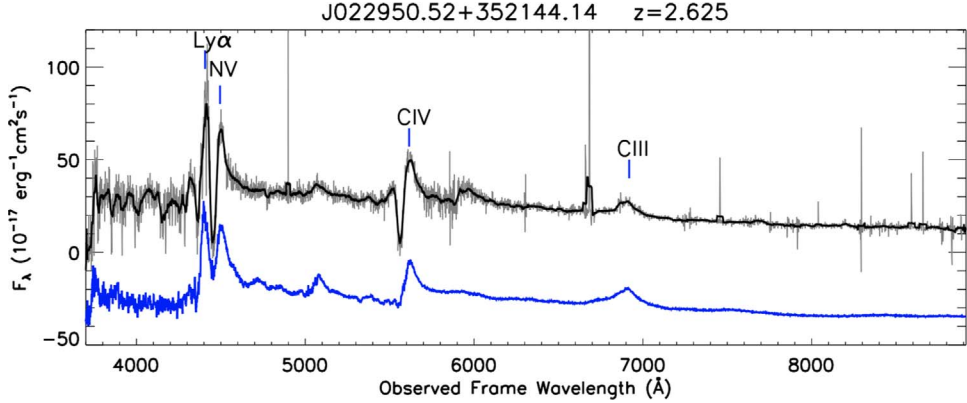


**Figure 18.** An example for the Ly $\alpha$  BAL quasar (black spectrum). The absorption features in the Ly $\alpha$  and C IV are obvious. The blue line is the BAL template spectra at the same redshift. There are no corrections for the redshift and Galactic extinction.

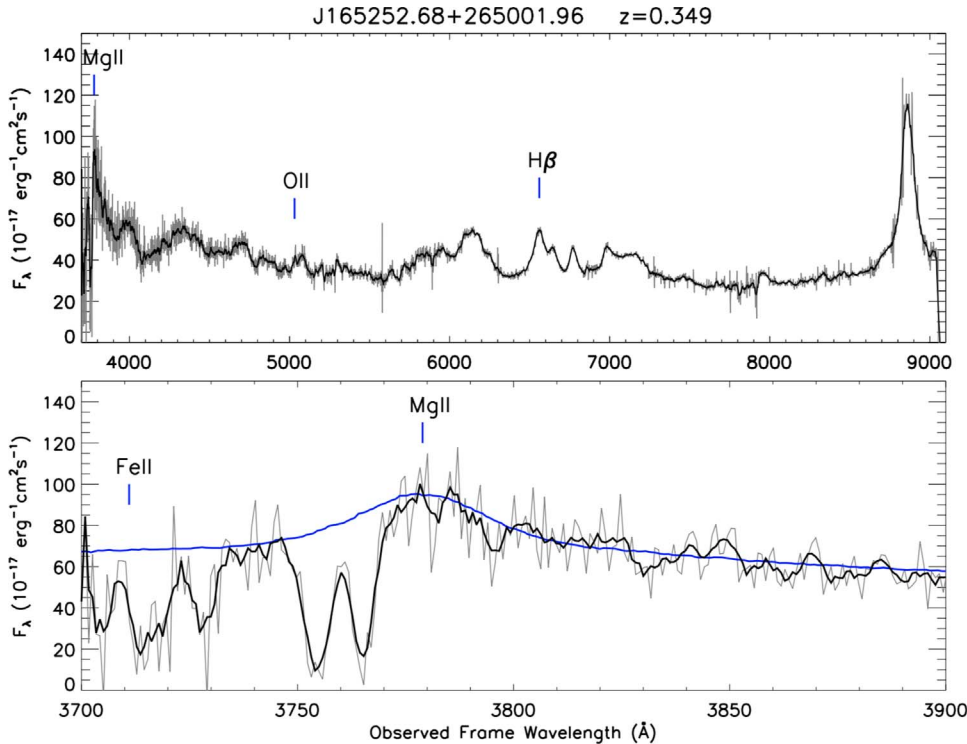


**Figure 19.** An example for the LoBAL quasar. The top panel shows the whole spectrum, and the bottom panel is a zoom-in near the Mg II region. The blue line is the normal quasar template spectra at the same redshift. The Mg II absorption features are clear. There are no corrections for the redshift and Galactic extinction.

in the LAMOST quasar survey have been presented previously (Yang et al. 2018), and follow-up works are ongoing.

Except CL-AGNs, LAMOST quasars also include other kinds of interesting, unusual quasars. Figure 18 presents the spectrum of an Ly $\alpha$  BAL quasar discovered during the visual inspection. Low-ionization BAL (LoBAL) quasars were also discovered in the survey. The spectrum of a LoBAL is plotted in Figure 19, where the Mg II absorption features are obvious.

The quasar catalog provided by LAMOST is not only a great supplement to the low-to-moderate-redshift quasars but also a large database for investigating the quasar spectral variabilities and searching for unusual quasars.

It is worthwhile to launch the follow-up studies for discovery and investigating these interesting quasars in the LAMOST quasar survey, such as the CL-AGN, BAL, and LoBAL. Meanwhile, the LAMOST ongoing survey will extend its

systematic searches to GPQs (Fu et al. 2021, 2022), which will provide more valuable data in the future.

This work is supported by the NSFC grants Nos. 11721303, 11927804, 12133001 and the Ministry of Science and Technology of China under grant 2016YFA0400703. The authors acknowledge the support by the China Postdoctoral Science Foundation (2021M690229), and the science research grant from the China Manned Space Project with No. CMS-CSST-2021-A06. Guoshoujing Telescope (the Large Sky Area Multi-Object Fiber Spectroscopic Telescope LAMOST) is a National Major Scientific Project built by the Chinese Academy of Sciences. Funding for the project has been provided by the National Development and Reform Commission. LAMOST is operated and managed by the National Astronomical Observatories, Chinese Academy of Sciences.

This publication makes use of data products from the Sloan Digital Sky Survey. Funding for the Sloan Digital Sky Survey IV has been provided by the Alfred P. Sloan Foundation, the U.S. Department of Energy Office of Science, and the Participating Institutions. SDSS-IV acknowledges support and resources from the Center for High-Performance Computing at the University of Utah. The SDSS website is [www.sdss.org](http://www.sdss.org). This work has made use of SDSS spectroscopic data. Funding for SDSS-III has been provided by the Alfred P. Sloan Foundation, the Participating Institutions, the National Science Foundation, and the U.S. Department of Energy Office of Science. The SDSS-III website is <http://www.sdss3.org/>. SDSS-III is managed by the Astrophysical Research Consortium for the Participating Institutions of the SDSS-III Collaboration, including the University of Arizona, the Brazilian Participation Group, Brookhaven National Laboratory, Carnegie Mellon University, University of Florida, the French Participation Group, the German Participation Group, Harvard University, the Instituto de Astrofísica de Canarias, the Michigan State/Notre Dame/JINA Participation Group, Johns Hopkins University, Lawrence Berkeley National Laboratory, Max Planck Institute for Astrophysics, Max Planck Institute for Extraterrestrial Physics, New Mexico State University, New York University, Ohio State University, Pennsylvania State University, University of Portsmouth, Princeton University, the Spanish Participation Group, University of Tokyo, University of Utah, Vanderbilt University, University of Virginia, University of Washington, and Yale University. The Pan-STARRS1 Surveys (PS1) and the PS1 public science archive have been made possible through contributions by the Institute for Astronomy, the University of Hawaii, the Pan-STARRS Project Office, the Max-Planck Society and its participating institutes, the Max Planck Institute for Astronomy, Heidelberg and the Max Planck Institute for Extraterrestrial Physics, Garching, The Johns Hopkins University, Durham University, the University of Edinburgh, the Queen's University Belfast, the Harvard-Smithsonian Center for Astrophysics, the Las Cumbres Observatory Global Telescope Network Incorporated, the National Central University of Taiwan, the Space Telescope Science Institute, the National Aeronautics and Space Administration under grant No. NNX08AR22G issued through the Planetary Science Division of the NASA Science Mission Directorate, the National Science Foundation grant No. AST-1238877, the University of Maryland, Eotvos Lorand University (ELTE), the Los Alamos National Laboratory, and the Gordon and Betty Moore Foundation.

## ORCID iDs

- Jun-Jie Jin  <https://orcid.org/0000-0002-8402-3722>  
 Xue-Bing Wu  <https://orcid.org/0000-0002-7350-6913>  
 Yuming Fu  <https://orcid.org/0000-0002-0759-0504>  
 Su Yao  <https://orcid.org/0000-0002-9728-1552>

## References

- Ahn, C. P., Alexandroff, R., Allende Prieto, C., et al. 2012, *ApJS*, 203, 21  
 Ai, Y. L., Wu, X.-B., Yang, J., et al. 2016, *AJ*, 151, 24  
 Andrei, A. H., Souchay, J., Zacharias, N., et al. 2009, *A&A*, 505, 385  
 Antonucci, R. 1993, *ARA&A*, 31, 473  
 Assef, R. J., Denney, K. D., Kochanek, C. S., et al. 2011, *ApJ*, 742, 93  
 Bailer-Jones, C. A. L., Fouesneau, M., & Andrae, R. 2019, *MNRAS*, 490, 5615  
 Becker, R. H., Fan, X., White, R. L., et al. 2001, *AJ*, 122, 2850  
 Boller, T., Freyberg, M. J., Trümper, J., et al. 2016, *A&A*, 588, A103  
 Boroson, T. 2005, *AJ*, 130, 381  
 Boroson, T. A., & Green, R. F. 1992, *ApJS*, 80, 109  
 Bovy, J., Hennawi, J. F., Hogg, D. W., et al. 2011, *ApJ*, 729, 141  
 Boyle, B. J., Shanks, T., Croom, S. M., et al. 2000, *MNRAS*, 317, 1014  
 Carballo, R., Cofino, A. S., & Gonzalez-Serrano, J. I. 2004, *MNRAS*, 353, 211  
 Chadid, M., Wade, G. A., Shorlin, S. L. S., et al. 2004, *A&A*, 413, 1087  
 Chambers, K. C., Magnier, E. A., Metcalfe, N., et al. 2016, arXiv:1612.05560  
 Clowes, R. G. 1986, *MitAG*, 67, 174  
 Coffey, D., Salvato, M., Merloni, A., et al. 2019, *A&A*, 625, A123  
 Cui, X.-Q., Zhao, Y.-H., Chu, Y.-Q., et al. 2012, *RAA*, 12, 1197  
 Cutri, R. M., et al. 2012, yCat, II/311  
 Denney, K. D. 2012, *ApJ*, 759, 44  
 Dong, X. Y., Wu, X.-B., Ai, Y. L., et al. 2018, *AJ*, 155, 189  
 Dye, S., Warren, S. J., Hambly, N. C., et al. 2006, *MNRAS*, 372, 1227  
 Elvis, M., Wilkes, B. J., McDowell, J. C., et al. 1994, *ApJS*, 95, 1  
 Fan, X. 1999, *AJ*, 117, 2528  
 Fan, X. Y., White, R. L., Davis, M., et al. 2000, *AJ*, 120, 1167  
 Feissel, M., & Mignard, F. 1998, *A&A*, 331, L33  
 Ferrarese, L., & Merritt, D. 2000, *ApJL*, 539, L9  
 Fitzpatrick, E. L. 1999, *PASP*, 111, 63  
 Flesch, E. W. 2021, arXiv:2105.12985  
 Flewelling, H. A., Magnier, E. A., Chambers, K. C., et al. 2020, *ApJS*, 251, 7  
 Frederick, S., Gezari, S., Graham, M. J., et al. 2019, *ApJ*, 883, 31  
 Fu, Y., Wu, X.-B., Jiang, L., et al. 2022, *ApJS*, 261, 32  
 Fu, Y., Wu, X.-B., Yang, Q., et al. 2021, *ApJS*, 254, 6  
 Fu, Y. 2021, QSOFITMORE: a python package for fitting UV-optical spectra of quasars, Zenodo, doi:10.5281/zenodo.5810042  
 Gebhardt, K., Bender, R., Bower, G., et al. 2000, *ApJL*, 539, L13  
 Guo, H., Shen, Y., & Wang, S. 2018, PyQSOFit: Python code to fit the spectrum of quasars, Astrophysics Source Code Library, ascl:1809.008  
 Guo, H., Sun, M., Liu, X., et al. 2019, *ApJL*, 883, L44  
 Heintz, K. E., Fynbo, J. P. U., Geier, S. J., et al. 2020, *A&A*, 644, A17  
 Hennawi, J. F., & Prochaska, J. X. 2007, *ApJ*, 655, 735  
 Hewett, P. C., Warren, S. J., Leggett, S. K., & Hodgkin, S. T. 2006, *MNRAS*, 367, 454  
 Huo, Z.-Y., Liu, X.-W., Xiang, M.-S., et al. 2013, *AJ*, 145, 159  
 Huo, Z.-Y., Liu, X.-W., Xiang, M.-S., et al. 2015, *RAA*, 15, 1438  
 Huo, Z.-Y., Liu, X.-W., Yuan, H.-B., et al. 2010, *RAA*, 10, 612  
 Jin, J.-J., Wu, X.-B., & Feng, X.-T. 2022, *ApJ*, 926, 184  
 Jin, X., Zhang, Y., Zhang, J., et al. 2019, *MNRAS*, 485, 4539  
 Komossa, S., & Xu, D. 2007, *ApJL*, 667, L33  
 Kormendy, J., & Gebhardt, K. 2001, in AIP Conf. Proc. 586, 20th Texas Symp. on Relativistic Astrophysics (Melville, NY: AIP), 363  
 Lawrence, A., Warren, S. J., Almaini, O., et al. 2007, *MNRAS*, 379, 1599  
 Li, J., Silverman, J. D., Ding, X., et al. 2021a, *ApJ*, 918, 22  
 Li, J., Silverman, J. D., Ding, X., et al. 2021b, *ApJ*, 922, 142  
 Luo, A.-L., Zhang, H.-T., Zhao, Y.-H., et al. 2012, *RAA*, 12, 1243  
 Luo, A.-L., Zhao, Y.-H., Zhao, G., et al. 2015, *RAA*, 15, 1095  
 Lyke, B. W., Higley, A. N., McLane, J. N., et al. 2020, *ApJS*, 250, 8  
 MacLeod, C. L., Green, P. J., Anderson, S. F., et al. 2019, *ApJ*, 874, 8  
 MacLeod, C. L., Ivezić, Ž., Sesar, B., et al. 2012, *ApJ*, 753, 106  
 MacLeod, C. L., Ross, N. P., Lawrence, A., et al. 2016, *MNRAS*, 457, 389  
 Maddox, N., Hewett, P. C., Warren, S. J., & Croom, S. M. 2008, *MNRAS*, 386, 1605  
 Magorrian, J., Tremaine, S., Richstone, D., et al. 1998, *AJ*, 115, 2285  
 Markwardt, C. B. 2009, in ASP Conf. Ser. 411, Astronomical Data Analysis Software and Systems XVIII, ed. D. A. Bohlender (San Francisco, CA: ASP), 251  
 Merritt, D., & Ferrarese, L. 2001, *MNRAS*, 320, L30  
 Morganson, E., Green, P. J., Anderson, S. F., et al. 2015, *ApJ*, 806, 244  
 Myers, A. D., Palanque-Delabrouille, N., Prakash, A., et al. 2015, *ApJS*, 221, 27  
 Palanque-Delabrouille, N., Magneville, C., Yèche, C., et al. 2016, *A&A*, 587, A41  
 Pâris, I., Petitjean, P., Aubourg, É., et al. 2012, *A&A*, 548, A66  
 Pâris, I., Petitjean, P., Aubourg, É., et al. 2018, *A&A*, 613, A51  
 Pasquet-Itam, J., & Pasquet, J. 2018, *A&A*, 611, A97  
 Peng, N., Zhang, Y., Zhao, Y., & Wu, X.-B. 2012, *MNRAS*, 425, 2599  
 Rakshit, S., Stalin, C. S., & Kotilainen, J. 2020, *ApJS*, 249, 17  
 Richards, G. T., Fan, X., Newberg, H. J., et al. 2002, *AJ*, 123, 2945  
 Richards, G. T., Myers, A. D., Gray, A. G., et al. 2009, *ApJS*, 180, 67  
 Richards, G. T., Nichol, R. C., Gray, A. G., et al. 2004, *ApJS*, 155, 257  
 Richards, G. T., Strauss, M. A., Fan, X., et al. 2006, *AJ*, 131, 2766  
 Robinson, L. B., & Wampler, E. J. 1972, *PASP*, 84, 161  
 Ross, N. P., Myers, A. D., Sheldon, E. S., et al. 2012, *ApJS*, 199, 3  
 Runco, J. N., Cosens, M., Bennert, V. N., et al. 2016, *ApJ*, 821, 33

- Salviander, S., Shields, G. A., Gebhardt, K., et al. 2007, *ApJ*, **662**, 131  
 Schlegel, D. J., Finkbeiner, D. P., & Davis, M. 1998, *ApJ*, **500**, 525  
 Schmidt, E. O., Oio, G. A., Ferreiro, D., et al. 2018, *A&A*, **615**, A13  
 Schmidt, M. 1963, *Natur*, **197**, 1040  
 Schneider, D. P., Hall, P. B., Richards, G. T., et al. 2007, *AJ*, **134**, 102  
 Serote Roos, M., Boisson, C., Joly, M., & Ward, M. J. 1998, *MNRAS*, **301**, 1  
 Sharp, R. G., Sabbe, C. N., Vivas, A. K., et al. 2002, *MNRAS*, **337**, 1153  
 Shen, Y., Hall, P. B., Horne, K., et al. 2019, *ApJS*, **241**, 34  
 Shen, Y., Richards, G. T., Strauss, M. A., et al. 2011, *ApJS*, **194**, 45  
 Shin, J., Nagao, T., Woo, J.-H., et al. 2019, *ApJ*, **874**, 22  
 Silverman, J. D., Green, P. J., Kim, D.-W., et al. 2002, *ApJL*, **569**, L1  
 Smail, I., Sharp, R., Swinbank, A. M., et al. 2008, *MNRAS*, **389**, 407  
 Song, Y.-H., Luo, A.-L., Comte, G., et al. 2012, *RAA*, **12**, 453  
 Su, D.-Q., & Cui, X. Q. 2004, *ChJAA*, **4**, 1  
 Trager, S. C., Worthey, G., Faber, S. M., et al. 1998, *ApJS*, **116**, 1  
 Tremaine, S., Gebhardt, K., Bender, R., et al. 2002, *ApJ*, **574**, 740  
 Tsuzuki, Y., Kawara, K., Yoshii, Y., et al. 2006, *ApJ*, **650**, 57  
 Vanden Berk, D. E., Richards, G. T., Bauer, A., et al. 2001, *AJ*, **122**, 549  
 Vestergaard, M., & Peterson, B. M. 2006, *ApJ*, **641**, 689  
 Vestergaard, M., & Wilkes, B. J. 2001, *ApJS*, **134**, 1  
 Wang, J., Xu, D. W., Wang, Y., et al. 2019, *ApJ*, **887**, 15  
 Wang, J.-G., Dong, X.-B., Wang, T.-G., et al. 2009, *ApJ*, **707**, 1334  
 Wang, S., Shen, Y., Jiang, L., et al. 2019, *ApJ*, **882**, 4  
 Wang, S.-G., Su, D. Q., Chu, Y.-Q., et al. 1996, *ApOpt*, **35**, 5155  
 Warren, S. J., Hewett, P. C., & Foltz, C. B. 2000, *MNRAS*, **312**, 827  
 Webb, N. A., Coriat, M., Traulsen, I., et al. 2020, *A&A*, **641**, A136  
 Wills, B. J., Netzer, H., & Wills, D. 1985, *ApJ*, **288**, 94  
 Worseck, G., Wisotzki, L., & Selman, F. 2008, *A&A*, **487**, 539  
 Wright, E. L., Eisenhardt, P. R. M., Mainzer, A. K., et al. 2010, *AJ*, **140**, 1868  
 Wu, X.-B., Hao, G., Jia, Z., et al. 2012, *AJ*, **144**, 49  
 Wu, X.-B., & Jia, Z. 2010, *MNRAS*, **406**, 1583  
 Xiang, M. S., Liu, X. W., Yuan, H. B., et al. 2015, *MNRAS*, **448**, 90  
 Yang, Q., Wu, X.-B., Fan, X., et al. 2018, *ApJ*, **862**, 109  
 Yao, S., Wu, X.-B., Ai, Y. L., et al. 2019, *ApJS*, **240**, 6  
 Yèche, C., Petitjean, P., Rich, J., et al. 2010, *A&A*, **523**, A14  
 York, D. G., Adelman, J., Anderson, J. E., et al. 2000, *AJ*, **120**, 1579  
 Yuan, H., Zhang, H., Zhang, Y., et al. 2013, *A&C*, **3**, 65  
 Zamfir, S., Sulentic, J. W., Marziani, P., & Dultzin, D. 2010, *MNRAS*, **403**, 1759  
 Zeimann, G. R., White, R. L., Becker, R. H., et al. 2011, *ApJ*, **736**, 57  
 Zhao, G., Zhao, Y.-H., Chu, Y.-Q., Jing, Y.-P., & Deng, L.-C. 2012, *RAA*, **12**, 723